drones

MDPI

Article

Fast Finite-Time Super-Twisting Sliding Mode Control with an Extended State Higher-Order Sliding Mode Observer for UUV Trajectory Tracking

Liwei Guo [1], Weidong Liu [1], Le Li [1,*], Jingming Xu [1], Kang Zhang [2] and Yuang Zhang [2]

[1] School of Marine Science and Technology, Northwestern Polytechnical University, Xi'an 710072, China; 2019100504@mail.nwpu.edu.cn (L.G.); liuwd@nwpu.edu.cn (W.L.); 2018260584@mail.nwpu.edu.cn (J.X.)
[2] The Second Wuhan Ship Design and Research Institute, Wuhan 430205, China; zhangkang62@buaa.edu.cn (K.Z.); 444984677@hrbeu.edu.cn (Y.Z.)
* Correspondence: leli@nwpu.edu.cn

Abstract: This paper proposes a trajectory tracking control scheme consisting of a fast finite-time super-twisting sliding mode control (FSTSMC) approach and an extended state higher-order sliding mode observer (ESHSMO) for unmanned underwater vehicles (UUVs) with external disturbances and model uncertainties. Firstly, an extended state higher-order sliding mode observer with the finite-time convergence is designed based on the higher-order sliding mode technique and the extended state observer technique. Next, on the basis of disturbances and model uncertainties observation, a fast finite-time super-twisting sliding mode control approach is proposed, and the finite time stabilization property of the tracking errors is proved by Lyapunov theory. Finally, through numerical simulation and experiment in a water pool, it has been verified that the proposed control scheme has achieved the high control precision, the smaller chattering, the disturbance compensation and the fast finite-time convergence in UUV trajectory tracking.

Keywords: unmanned underwater vehicle; super-twisting sliding mode control; extended state higher-order sliding mode observer; fast finite-time convergence

check for updates

Citation: Guo, L.; Liu, W.; Li, L.; Xu, J.; Zhang, K.; Zhang, Y. Fast Finite-Time Super-Twisting Sliding Mode Control with an Extended State Higher-Order Sliding Mode Observer for UUV Trajectory Tracking. *Drones* **2024**, *8*, 41. https://doi.org/10.3390/drones8020041

Academic Editor: Emmanouel T. Michailidis

Received: 2 December 2023
Revised: 20 January 2024
Accepted: 24 January 2024
Published: 30 January 2024

Copyright: © 2024 by the authors. Licensee MDPI, Basel, Switzerland. This article is an open access article distributed under the terms and conditions of the Creative Commons Attribution (CC BY) license (https://creativecommons.org/licenses/by/4.0/).

1. Introduction

UUVs have become important tools in a wide range of ocean observation and exploration missions, including marine environment monitoring, mineral resources exploration, and underwater rescue. The successful execution of these missions requires the UUVs with accurate trajectory tracking control performance. However, unknown external disturbances such as ocean currents and model uncertainties hinder the traditional linear control approaches from achieving the required tracking control performance.

A tremendous amount of research efforts has been spent on the development and test of advanced control approaches for unmanned vehicles, such as sliding mode control [1–8], model predictive control [9–12], backstepping control [13–17], active disturbance rejection control [18–21], adaptive control [22–25] and fixed-time control [26–28]. Among them, sliding mode control has shown excellent robustness to external disturbances and model uncertainties, and it is convenient in the design and debugging of control parameters. However, the output of traditional sliding mode approach contains discontinuous switching items, which results in chattering phenomenon. The chattering is an inherent defect of conventional sliding mode control, which increases energy consumption, damages thrusters and stimulates unmodeled dynamics. The quasi-sliding mode control methods use continuous functions such as saturation function, hyperbolic tangent function and arctangent function instead of sign function to weaken chattering [29–31]. These quasi-sliding mode control approaches are typically at the cost of losing the robustness or control precision, which is harmful to the accurate trajectory tracking control of UUVs.

Levant introduced the concept of higher-order sliding mode control, which overcomes the inherent defects of conventional sliding mode control without degrading control performance [32]. The output of the higher-order sliding mode control does not directly contain the sign function but rather the integral of the sign function. In this way, the higher-order sliding mode control is continuous, which can eliminate the chattering of control quantity and can ensure good robustness. The high-order sliding mode control algorithm mainly includes the twisting algorithm, the super-twisting algorithm, the prescribed convergence law algorithm, the sub-optimal algorithm and so on. Among them, the super-twisting algorithm plays an important role in the higher-order sliding mode control, because it does not need to know the derivative information of sliding mode variables in advance, and it is relatively easy to design Lyapunov functions to prove finite-time stability. Borlaug et al. used the adaptive gain super-twisting control approach and the generalized super-twisting control approach in an articulated intervention autonomous underwater vehicle to perform trajectory tracking [33]. Experiment results showed that the adaptive gain super-twisting control approach and the generalized super-twisting control approach have good tracking performance compared with PID control approach in terms of convergence speed and steady-state error. Manzanilla et al. combined integral sliding mode control technology and super-twisting control technology to design a robust sliding mode control method for the 3D trajectory tracking of underwater vehicle, which significantly attenuated chattering and verified its robustness against bounded disturbances [34]. González-García et al. presented a model-free super-twisting control method with finite-time convergence for AUV trajectory tracking, and compared it with PID control method and conventional sliding mode control method [35]. The results showed that the model-free super-twisting algorithm has obvious advantages in steady-state errors and the energy consumption of actuators. This paper proposes a fast finite-time super-twisting sliding mode control approach to inherit the advantages of high-order sliding mode, such as strong robustness, finite time convergence, and weakening chattering. Moreover, compared with the references mentioned above, the proposed fast finite-time super-twisting sliding mode control approach has the following novel aspects. Firstly, a smooth sliding mode reaching law is designed to effectively weaken chattering, and a fast term is introduced to make the sliding mode variables converge quickly in finite time. Secondly, the control scheme in this paper combines the extended observer with the sliding mode control approach. This scheme not only fully considers the information from the nominal model of the UUV but also effectively eliminates the uncertainty of the model and eliminate the dependence on the exact model. The observer can effectively reduce the control gain and further improve the control performance. Thirdly, the complete proof of fast finite-time convergence of the control scheme is given. Finally, the control scheme is verified through simulation and experiment.

In addition, it is generally known that the robustness of sliding mode control to unknown external disturbances and model uncertainties depends on the control gain. The increase of the control gain will improve the robustness but will also require a higher energy consumption, even stimulate the unmodeled characteristics, and affect the control performance. Therefore, the extended state observer (ESO) technique that can approximate the unknown disturbances needs to be introduced into the trajectory tracking task to reduce the control gain and to improve the control performance. Li et al. designed the ESO to estimate parameter perturbations and external disturbances for the precise trajectory tracking control problem of UUVs [36]. Wu et al. combined the iterative ESO with the model-free adaptive control method, and the proposed controller could estimate and compensate the unknown errors caused by external environmental disturbances [37]. Lamraoui et al. used the generalized ESO and the harmonic ESO to estimate the fast-varying disturbances caused by waves and ocean currents [19]. Moreover, ESO increases the bandwidth of the observer to reduce the observation error, speed up the convergence, and enhance the robustness. However, an excessively high bandwidth will magnify the effects of high-frequency noise and impair the control performance of the system. Kim

proposed a sliding mode observer to accelerate convergence for large-amplitude external disturbances and model uncertainties, and they verified the performance of the control system through numerical simulation [38]. Nevertheless, a chattering phenomenon still exists in the observer output and further damages the system stability when directly using the sliding mode observer. In order to accelerate the observation convergence speed and improve the observation precision while avoiding the introduction of high-frequency disturbances and chattering, this paper proposes an extended state higher-order sliding mode observer.

To sum up, this paper proposes a trajectory tracking control scheme consist of a fast finite-time super-twisting sliding mode control approach (FSTSMC) and an extended state higher-order sliding mode observer (ESHSMO) for UUVs with external disturbances and model uncertainties. The main contributions of this paper are as follows:

(1) A fast finite-time super-twisting sliding mode control approach is proposed for the UUV trajectory tracking to attenuate chattering and enhance robustness. A linear term is added to accelerate the convergence when the sliding modulus is far from the sliding mode surface. The finite-time stabilization property is proved through using Lyapunov function.

(2) By integrating the high-order sliding mode technique into the extended state observer technique, the ESHSMO is designed to enhance the observation precision, to accelerate the convergence speed of observation errors, and to attenuate the observation output chattering. The finite-time convergence property of the ESHSMO is proved.

(3) Numerical simulation and experiment in the water pool verify that the proposed scheme shows good trajectory tracking control performance with higher control precision, smaller chattering, stronger disturbance compensation and faster finite-time convergence.

2. Uuv Modeling and Problem Formulation

The notations and lemmas that will be used in the rest of the paper are listed in Sections 2.1 and 2.2. The kinematics model, the dynamics model, and the thrust distribution matrix of UUV are presented next, respectively, in Sections 2.3–2.5.

2.1. Notations

For vector, $|\boldsymbol{f}|^g = diag(|f_1|^g, \ldots, |f_n|^g)$, $\mathrm{sgn}(\boldsymbol{f}) = [\mathrm{sgn}(f_1), \ldots, \mathrm{sgn}(f_n)]^T$; where sgn represents the standard sign function; $\lceil \boldsymbol{f} \rfloor^g = |\boldsymbol{f}|^g \mathrm{sgn}(\boldsymbol{f})$. $\min_{i=1,\ldots,n}(f_i)$ and $\max_{i=1,\ldots,n}(f_i)$ represent the minimum and maximum elements in $\boldsymbol{f}$, respectively, and $\|\boldsymbol{f}\|$ represents the Euclidean norm, which can be calculated by $\|\boldsymbol{f}\| = \sqrt{\boldsymbol{f}^T\boldsymbol{f}}$. For matrix $\boldsymbol{F}$, $\|\boldsymbol{F}\|$ represents the Frobenius norm, which can be calculated by $\|\boldsymbol{F}\| = \sqrt{tr(\boldsymbol{F}^T\boldsymbol{F})}$, $\lambda_{\min}(\boldsymbol{F})$ and $\lambda_{\max}(\boldsymbol{F})$ represent the minimum and maximum eigenvalues, respectively. $\boldsymbol{I}_{n\times n}$ represents the identity matrix of order $n \times n$ and $\boldsymbol{0}_{m\times n}$ represents the zero matrix of order $m \times n$.

2.2. Lemmas

This section presents the relevant lemmas used in the proof of ESHSMO and FSTSMC.

Lemma 1 (Lyapunov Matrix Equation)**.** *If all eigenvalues of matrix $\bar{\boldsymbol{A}}$ have negative real parts, then for any given symmetric positive definite matrix $\boldsymbol{\Lambda} = \begin{bmatrix} \boldsymbol{\Lambda}_1 & \boldsymbol{0}_{12\times 12} \\ \boldsymbol{0}_{12\times 12} & \boldsymbol{\Lambda}_2 \end{bmatrix}$, there exists a symmetric positive definite matrix $\boldsymbol{P}$ such that $\bar{\boldsymbol{A}}^T\boldsymbol{P} + \boldsymbol{P}\bar{\boldsymbol{A}} = -\boldsymbol{\Lambda}$ holds.*

Lemma 2 ([39])**.** *Consider the following nonlinear system:*

$$\dot{\boldsymbol{x}} = \boldsymbol{f}(\boldsymbol{x}) \tag{1}$$

where $\boldsymbol{f}(\boldsymbol{0}) = \boldsymbol{0}$, $\boldsymbol{x} \in R^n$, $\boldsymbol{f} : U_0 \to R^n$ is a continuous function in an open neighborhood U_0 containing the origin. Suppose there is a continuous positive definite function $V(x) : U_0 \to R^n$, and there are real numbers $c, b > 0$, $0 < a < 1$ and $\kappa \in (0, b)$, so that the following equation holds:

$$\dot{V} \leq -bV + cV^a < 0 \tag{2}$$

Then, the system (1) *is fast finite time uniformly bounded stable with stability domain* $Q = \left\{ \boldsymbol{x} : V < \left(\frac{c}{\kappa}\right)^{\frac{1}{1-a}} \right\}$ *and the convergence time satisfies* $T_{(x_0)} \leq \frac{1}{b(1-a)} \ln\left(\frac{bV_{(x_0)} - c}{bc/\kappa - c} \right)$.

Lemma 3 ([40]). *Considering the nonlinear system* (1)*, it is assumed that there is a continuous positive definite function* $V(x) : U_0 \to R^n$ *with real numbers* $c, b > 0$ *and* $0 < a < 1$*, and an open neighborhood* $\hat{U} \subseteq U_0$ *containing the origin, such that the following equation holds:*

$$\dot{V} \leq -bV - cV^a, x \in \hat{U} \backslash \{0\} \tag{3}$$

Then, the origin of the system (1) *is stable in finite time, and the stabilization time T depends on the initial value* x_0*, such that* $T_{(x_0)} \leq \frac{\ln\left(1 + \frac{b}{c} V_{(x_0)}^{1-a}\right)}{b(1-a)}$*, and if* $\hat{U} = U_0 = \mathrm{R}^n$*, the origin of the system* (1) *is globally stable in finite time.*

Lemma 4 ([40]). *Considering the nonlinear system* (1)*, it is assumed that there is a continuous positive definite function* $V(\boldsymbol{x}) : U_0 \to R^n$*, and there are real numbers* $b, c, d > 0$*,* $0 < a < 0.5$ *and* $\kappa_1 \in (0, b)$*,* $\kappa_2 \in (0, c)$*, so that the following equation holds:*

$$\dot{V} \leq -bV^a - cV + dV^{\frac{1}{2}} < 0 \tag{4}$$

Then, the system (1) *is fast finite time uniformly bounded stable with stability domain* $Q = \left\{ \boldsymbol{x} : \kappa_1 V^{a-\frac{1}{2}} + \kappa_2 V^{\frac{1}{2}} < d \right\}$ *and the convergence time of the system satisfies* $T_{(x_0)} \leq \frac{1}{(c-\kappa_2)1-a)} \ln\left(\frac{(c-\kappa_2)V_{(x_0)}^{1-a} + b - \kappa_1}{b - \kappa_1} \right)$.

2.3. UUV Kinematics

In order to describe the 6-DOF spatial motion of UUV, the inertial coordinate system I and the body coordinate system B as shown in Figure 1 are defined. The parameter symbols in [41] are adopted in this paper, where $\boldsymbol{\eta} = [x, \mathrm{y}, \mathrm{z}, \phi, \theta, \varphi]^T$ represents the position and orientation of UUV in the inertial coordinate system and the body coordinate system; $\boldsymbol{v} = [u, v, w, p, q, r]^T$ represents the linear and angular velocity of UUV in the body coordinate system. Under ideal conditions, the kinematic model of UUV is described by the following equation:

$$\dot{\boldsymbol{\eta}} = \boldsymbol{J}(\boldsymbol{\eta})\boldsymbol{v} \tag{5}$$

The rotation matrix $\boldsymbol{J}(\eta)$ describes the velocity transformation between the inertial coordinate system and the body coordinate system. However, when UUV performs its actual tasks, the velocity of the ocean current fluid may not be negligible. After considering the influence of ocean current flow field, Equation (6) is modified as:

$$\dot{\boldsymbol{\eta}} = \boldsymbol{J}(\boldsymbol{\eta})\boldsymbol{v}_r + \boldsymbol{v}_f \tag{6}$$

where $\boldsymbol{v}_r$ represents the velocity vector of UUV relative to the fluid motion in the body coordinate system; $\boldsymbol{v}_f$ represents the velocity vector of the ocean current in the inertial coordinate system. The relationship between ocean current velocity $\boldsymbol{v}_f$, relative velocity $\boldsymbol{v}_r$ of UUV to ocean current and generalized velocity $\boldsymbol{v}$ is described as:

$$\begin{cases} \dot{\boldsymbol{\eta}} = \boldsymbol{J}(\boldsymbol{\eta})\boldsymbol{v}_r + \boldsymbol{v}_f \\ \boldsymbol{v} = \boldsymbol{v}_r + \boldsymbol{v}_c \\ \boldsymbol{v}_f = \boldsymbol{J}(\boldsymbol{\eta})\boldsymbol{v}_c \end{cases} \tag{7}$$

where $\boldsymbol{v}_c$ is the velocity of ocean current in the body coordinate system B. In general, only the velocity $\boldsymbol{v}_r$ of UUV relative to the current can be obtained, while the ocean current velocity $\boldsymbol{v}_f$ is unknown and needs to be compensated or estimated. According to the

relevant studies on ocean flow [42], the moving velocity and velocity change rate of fluid need to meet the law of energy conservation, and the moving velocity of fluid will not be infinite nor will the change rate of velocity. Therefore, the following reasonable assumptions are made for ocean flow velocity:

Assumption 1. *The current velocity $\boldsymbol{v}_f$ satisfies the bounded condition $\left\|\boldsymbol{v}_f\right\| \leq k_f$ and k_f is a certain constant.*

Assumption 2. *The derivative of current velocity $\dot{\boldsymbol{v}}_f$ satisfies the bounded condition $\left\|\dot{\boldsymbol{v}}_f\right\| \leq k_{df}$ and k_{df} is a certain constant.*

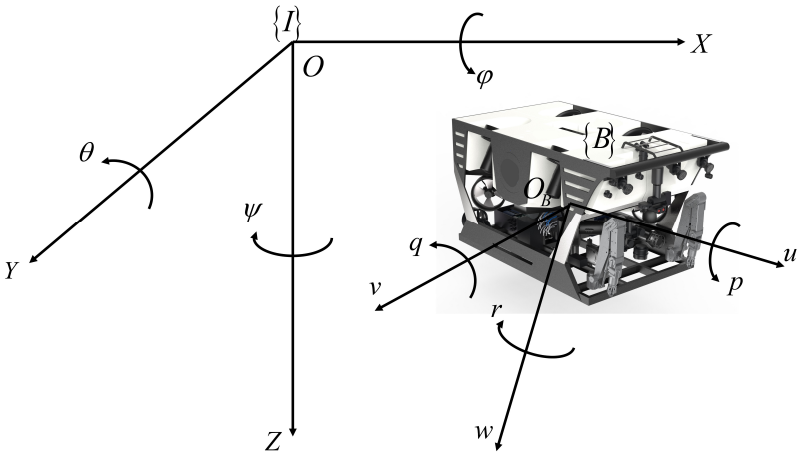


Figure 1. The inertial coordinate system I and the body coordinate system B.

2.4. UUV Dynamics

The dynamic equation of UUV can be expressed as:

$$\boldsymbol{M}\dot{\boldsymbol{v}}_r + \boldsymbol{C}(\boldsymbol{v}_r)\boldsymbol{v}_r + \boldsymbol{D}(\boldsymbol{v}_r)\boldsymbol{v}_r + \boldsymbol{g}(\boldsymbol{\eta}) = \boldsymbol{\tau}_T + \boldsymbol{\tau}_E \tag{8}$$

where $\boldsymbol{M}$ represents the inertia matrix, $\boldsymbol{C}$ represents the Coriolis force and centripetal force matrix, $\boldsymbol{D}$ represents the damping matrix, $\boldsymbol{g}$ represents the restoring force vector, $\boldsymbol{\tau}_E$ represents the unknown time-varying external disturbance force vector, and $\boldsymbol{\tau}_T$ represents the control force and torque vector. The above hydrodynamic parameters were calculated and analyzed in the experiment. When UUV is operated in a real ocean environment, the hydrodynamic parameters obtained by the experimental analysis are deviated from the actual hydrodynamic parameters. It can be seen from the above that it is not practical to establish a complete and undifferentiated dynamic model at present, and the model uncertainties need to be compensated. Therefore, the actual value $\boldsymbol{X}(\cdot)$ of the hydrodynamic parameter can be divided into the known nominal term $\boldsymbol{X}_0(\cdot)$ and the unknown uncertain term $\Delta\boldsymbol{X}(\cdot)$, which is expressed as $\boldsymbol{X}(\cdot) = \boldsymbol{X}_0(\cdot) + \Delta\boldsymbol{X}(\cdot), \boldsymbol{X} = \boldsymbol{M}, \boldsymbol{C}, \boldsymbol{D}, \boldsymbol{g}$. That is, the model uncertainty vector in UUV dynamics can be expressed as $\boldsymbol{\tau}_M = \Delta\boldsymbol{M}\dot{\boldsymbol{v}}_r + \Delta\boldsymbol{C}(\boldsymbol{v}_r)\boldsymbol{v}_r + \Delta\boldsymbol{D}(\boldsymbol{v}_r)\boldsymbol{v}_r + \Delta\boldsymbol{g}(\boldsymbol{\eta})$. To sum up, Equation (4) can be rewritten as:

$$\boldsymbol{M}_0\dot{\boldsymbol{v}}_r + \boldsymbol{C}_0(\boldsymbol{v}_r)\boldsymbol{v}_r + \boldsymbol{D}_0(\boldsymbol{v}_r)\boldsymbol{v}_r + \boldsymbol{g}_0(\boldsymbol{\eta}) = \boldsymbol{\tau}_T + \boldsymbol{\tau}_D \tag{9}$$

where $\boldsymbol{\tau}_D = \boldsymbol{\tau}_E + \boldsymbol{\tau}_M$ represents the lumped disturbance vector of the dynamics, including the model uncertainty term $\boldsymbol{\tau}_M$ and the external disturbance term $\boldsymbol{\tau}_E$.

Assumption 3. *The lumped disturbance $\boldsymbol{\tau}_D$ satisfies the bounded condition $\|\boldsymbol{\tau}_D\| \leq k_D$ and k_D is a certain constant.*

Assumption 4. *The derivative of lumped disturbance $\dot{\boldsymbol{\tau}}_D$ satisfies the bounded condition $\|\dot{\boldsymbol{\tau}}_D\| \leq k_{dD}$ and k_{dD} is a certain constant.*

2.5. Thrust Forces Distribution

The power system of the UUV consists of four horizontal thrusters and four vertical thrusters. The forces generated by the horizontal thrusters drive the UUV for longitudinal, lateral and course control. The forces generated by the vertical thrusters drive the UUV to control roll, pitch, and vertical motion. The relationship between the control force/torque of each degree of freedom and thrust of each thruster is described as follows:

$$\boldsymbol{\tau}_T = \boldsymbol{B}\boldsymbol{u} \tag{10}$$

where $\boldsymbol{u}$ represents the thrust vector generated by each thruster, and $\boldsymbol{B}$ represents the thrust distribution matrix. Because thrusters can only provide limited thrust, the saturation nonlinear characteristics of thrusters should be considered in practical application.

2.6. Control Objectives

The first objective of the paper is to design a finite-time convergence observer to estimate the model uncertainty $\boldsymbol{\tau}_M$ and the external disturbance $\boldsymbol{\tau}_D$. The next objective is to design a fast finite-time super-twisting sliding mode control approach to complete the high-precision trajectory tracking task combined with the observer. The control scheme in this paper consists of the control approach and the observer.

3. Extended State Higher-Order Sliding Mode Observer

In this section, the extended-state higher-order sliding mode observer is designed based on the extended state observer technique and the higher-order sliding mode technique. Meanwhile, the finite time convergence of the extended state higher-order sliding mode observer is proved.

3.1. Design of ESHSMO

Combined with UUV kinematics and the dynamics model described above, ocean current velocity vector $\boldsymbol{v}_f$ and lumped disturbance vector $\boldsymbol{\tau}_D$ are taken as extended states, and the extended state space expression of the system can be obtained:

$$\begin{bmatrix}\dot{\boldsymbol{x}}_1\\ \dot{\boldsymbol{x}}_2\end{bmatrix} = \begin{bmatrix}\boldsymbol{0}_{12\times12}\boldsymbol{I}_{12\times12}\\ \boldsymbol{0}_{12\times12}\boldsymbol{0}_{12\times12}\end{bmatrix}\begin{bmatrix}\boldsymbol{x}_1\\ \boldsymbol{x}_2\end{bmatrix} + \begin{bmatrix}\boldsymbol{f}_1(\boldsymbol{x}_1)\\ \boldsymbol{0}_{12\times1}\end{bmatrix} + \begin{bmatrix}\boldsymbol{0}_{12\times1}\\ \dot{\boldsymbol{x}}_2\end{bmatrix} + \begin{bmatrix}\boldsymbol{h}\boldsymbol{u}(t)\\ \boldsymbol{0}_{12\times1}\end{bmatrix} \tag{11}$$

In Equation (11), $\boldsymbol{x} = \left[\boldsymbol{x}_1^T, \boldsymbol{x}_2^T\right]^T$, where $\boldsymbol{x}_1 = \left[\boldsymbol{\eta}^T, \boldsymbol{v}_r^T\right]^T$ is the state vector of the system, which is the known quantity in the system and can be obtained directly by the sensor. $\boldsymbol{x}_2 = \left[\boldsymbol{v}_f^T, \boldsymbol{\tau}_{MD}^T\right]^T$ is the extended state vector of the system, which belongs to the unknown quantity of the system and needs to be estimated by the observer, $\boldsymbol{\tau}_{MD} = \boldsymbol{M}^{-1}\boldsymbol{\tau}_D$. $\boldsymbol{f}_1(\boldsymbol{x}_1) = \left[\boldsymbol{J}(\boldsymbol{\eta})\boldsymbol{v}_r, -\boldsymbol{M}_0^{-1}\boldsymbol{f}(\boldsymbol{v}_r, \boldsymbol{\eta})\right]^T$ is the known vector of the system, where $\boldsymbol{f}(\boldsymbol{v}_r, \boldsymbol{\eta}) = \boldsymbol{C}_0(\boldsymbol{v}_r)\boldsymbol{v}_r + \boldsymbol{D}_0(\boldsymbol{v}_r)\boldsymbol{v}_r + \boldsymbol{g}_0(\boldsymbol{\eta})$. $\boldsymbol{h} = \left[\boldsymbol{0}_{6\times6}, \boldsymbol{M}_0^{-1}\right]^T$ is the known matrix of the system. $\boldsymbol{u}(t) = \boldsymbol{\tau}_T$ represents the system control input and $\boldsymbol{y}$ represents the system state output.

Assumption 5. *The elements inside the state vector $\boldsymbol{x}_1$, $\boldsymbol{x}_2$ and the matrix function $\boldsymbol{f}_1(\boldsymbol{x}_1)$ are bounded. The nonlinear elements in the matrix function $\boldsymbol{f}_1(\boldsymbol{x}_1)$ all satisfy the Lipschitz condition, that is, any two independent variables $\boldsymbol{a}_1$ and $\boldsymbol{a}_2$ in the domain of definition must satisfy $\|\boldsymbol{f}_1(\boldsymbol{a}_2) - \boldsymbol{f}_1(\boldsymbol{a}_1)\| \leq L_k\|\boldsymbol{a}_2 - \boldsymbol{a}_1\|$, L_k is a constant greater than zero.*

For the uncertainties of ocean current velocity v_f and the lumped disturbance τ_D in the extended state Equation (11) of the system, the extended state higher-order sliding mode observer is designed as:

$$\begin{bmatrix}\dot{\hat{x}}_1\\ \dot{\hat{x}}_2\end{bmatrix} = \begin{bmatrix}\mathbf{0}_{12\times12}\mathbf{I}_{12\times12}\\ \mathbf{0}_{12\times12}\mathbf{0}_{12\times12}\end{bmatrix}\begin{bmatrix}\hat{x}_1\\ \hat{x}_2\end{bmatrix} + \begin{bmatrix}f_1(\hat{x}_1)\\ \mathbf{0}_{12\times1}\end{bmatrix} + \begin{bmatrix}hu(t)\\ \mathbf{0}_{12\times1}\end{bmatrix} + L[x_1-\hat{x}_1] + \Xi \tag{12}$$

In Equation (12): $\hat{x} = \left[\hat{x}_1^T, \hat{x}_2^T\right]^T$ is the state vector of ESHSMO, which represents the estimated value of the system state vector x, where $\hat{x}_1$ is the estimated value of x_1, and $\hat{x}_2$ is the estimated value of x_2. $L = \begin{bmatrix}l_1\mathbf{I}_{12\times12}\\ l_2\mathbf{I}_{12\times12}\end{bmatrix}$ is the observation error feedback gain matrix, where l_1, l_2 are specific positive real numbers. $\Xi = \begin{bmatrix}\beta_1\mathrm{sgn}(x_1-\hat{x}_1)\\ \beta_2\mathrm{sgn}(x_1-\hat{x}_1)+\beta_3\int_0^t\mathrm{sgn}(x_1-\hat{x}_1)d\tau\end{bmatrix}$ is the observer higher-order sliding mode matrix, where β_1, β_2 and β_3 are specific positive real numbers.

3.2. Convergence Analysis of ESHSMO

Theorem 1. *For the system (11) described above, ESHSMO designed in Equation (12) can realize the estimation of* $x = \left[x_1^T, x_2^T\right]^T$ *within a finite time.*

Proof. By combining the system extended state Equation (11) and ESHSMO Equation (12), the estimated error state equation can be obtained:

$$\begin{bmatrix}\dot{e}_1\\ \dot{e}_2\end{bmatrix} = \begin{bmatrix}-l_1\mathbf{I}_{12\times12}\mathbf{I}_{12\times12}\\ -l_2\mathbf{I}_{12\times12}\mathbf{0}_{12\times12}\end{bmatrix}\begin{bmatrix}e_1\\ e_2\end{bmatrix} + \begin{bmatrix}f_{e1}\\ \mathbf{0}_{12\times1}\end{bmatrix} + \begin{bmatrix}\mathbf{0}_{12\times1}\\ \dot{x}_2\end{bmatrix} - \begin{bmatrix}\beta_1\mathrm{sgn}(e_1)\\ \beta_2\mathrm{sgn}(e_1)+\beta_3\int_0^t\mathrm{sgn}(e_1)d\tau\end{bmatrix} \tag{13}$$

where $f_{e1} = f_1(x_1) - f_1(\hat{x}_1)$. For convenience, it can be rewritten as:

$$\dot{e} = \bar{A}e + \bar{F} + \bar{D} - \bar{B} \tag{14}$$

where $e = \left[e_1^T, e_2^T\right]^T$, $\bar{A} = \begin{bmatrix}-l_1\mathbf{I}_{12\times12} & \mathbf{I}_{12\times12}\\ -l_2\mathbf{I}_{12\times12} & \mathbf{0}_{12\times12}\end{bmatrix}$, $\bar{F} = \begin{bmatrix}f_{e1}\\ \mathbf{0}_{12\times1}\end{bmatrix}$, $\bar{D} = \begin{bmatrix}\mathbf{0}_{12\times1}\\ \dot{x}_2\end{bmatrix}$, $\bar{B} = \begin{bmatrix}\beta_1\mathrm{sgn}(e_1)\\ \beta_2\mathrm{sgn}(e_1)+\beta_3\int_0^t\mathrm{sgn}(e_1)d\tau\end{bmatrix}$. Take l_1, l_2 so that $\bar{A}$ is the Hurwitz matrix.

The Lyapunov function is designed according to Lemma 1. Firstly, select a diagonal matrix Λ whose elements are all greater than zero. Then, take the matrix $\bar{A}$ into Lemma 1 and calculate P that satisfies the condition.

$$P = \begin{bmatrix}P_{11} & P_{12}\\ P_{21} & P_{22}\end{bmatrix} = \begin{bmatrix}\frac{1}{2}l_1^{-1}\Lambda_1 + \frac{1}{2}l_1^{-1}l_2\Lambda_2 & -\frac{1}{2}\Lambda_2\\ -\frac{1}{2}\Lambda_2 & \frac{1}{2}l_1^{-1}l_2^{-1}\Lambda_1 + \left(\frac{1}{2}l_1^{-1} + \frac{1}{2}l_1l_2^{-1}\right)\Lambda_2\end{bmatrix} \tag{15}$$

Set the Lyapunov function V_0 of ESHSMO as

$$V_0 = e^TPe \tag{16}$$

Its time derivative is

$$\dot{V}_0 = e^TP\dot{e} + \dot{e}^TPe \tag{17}$$

Substituting Equation (15) into Equation (17), we can obtain

$$\begin{aligned}\dot{V}_o &= e^T\left(P\bar{A} + \bar{A}^TP\right)e + 2e^TP\bar{F} + 2e^TP\bar{D} - 2e^TP\bar{B}\\ &= -e^T\Lambda e + 2e^TP\bar{F} + 2e^TP\bar{D} - 2e^TP\bar{B}\end{aligned} \tag{18}$$

where

$$-\boldsymbol{e}^T\boldsymbol{\Lambda}\boldsymbol{e} \le -\lambda_{\min}(\boldsymbol{\Lambda})\|\boldsymbol{e}\|^2 \tag{19}$$

According to the basic inequality $2\boldsymbol{X}^T\boldsymbol{Y} \le \frac{1}{\varepsilon}\boldsymbol{X}^T\boldsymbol{X} + \varepsilon\boldsymbol{Y}^T\boldsymbol{Y}$, where $\varepsilon > 0$, $\boldsymbol{X}$ and $\boldsymbol{Y}$ are matrices of corresponding dimensions, it can be known that

$$2\boldsymbol{e}^T\boldsymbol{P}\bar{\boldsymbol{F}} \le \frac{1}{\varepsilon}\boldsymbol{e}^T\boldsymbol{P}\boldsymbol{P}\boldsymbol{e} + \varepsilon\bar{\boldsymbol{F}}^T\bar{\boldsymbol{F}} \tag{20}$$

According to Assumption 5, it can be obtained

$$\boldsymbol{F}^T\boldsymbol{F} = \|\boldsymbol{f}_1(\boldsymbol{x}_1) - \boldsymbol{f}_1(\hat{\boldsymbol{x}}_1)\|^2 \le L_k\|\boldsymbol{x}_1 - \hat{\boldsymbol{x}}_1\|^2 \le L_k\|\boldsymbol{e}\|^2 \tag{21}$$

Substitute Equation (21) into Equation (20) and obtain

$$2\boldsymbol{e}^T\boldsymbol{P}\bar{\boldsymbol{F}} \le \left(\frac{1}{\varepsilon}\|\boldsymbol{P}\|^2 + \varepsilon L_k\right)\|\boldsymbol{e}\|^2 \tag{22}$$

According to Assumptions 2 and 4, it can be known that $\left\|\dot{\boldsymbol{v}}_f\right\| \le k_{df}$, $\|\dot{\boldsymbol{\tau}}_{MD}\| \le \left\|\boldsymbol{M}_0^{-1}\right\|$ $\|\dot{\boldsymbol{\tau}}_D\| \le k_{dD}\left\|\boldsymbol{M}_0^{-1}\right\|$. Thus, $\|\bar{\boldsymbol{D}}\| \le \left\|\begin{matrix} k_{df} \\ k_{dD}\left\|\boldsymbol{M}_0^{-1}\right\| \end{matrix}\right\| = M_D$, then

$$2\boldsymbol{e}^T\boldsymbol{P}\bar{\boldsymbol{D}} \le 2M_D\|\boldsymbol{P}\|\|\boldsymbol{e}\| \tag{23}$$

Meanwhile, Equation (24) can be obtained:

$$\begin{aligned}
&-2\boldsymbol{e}^T\boldsymbol{P}\bar{\boldsymbol{B}} \\
&= -2\begin{bmatrix}\boldsymbol{e}_1^T & \boldsymbol{e}_2^T\end{bmatrix}\begin{bmatrix}\boldsymbol{P}_{11} & \boldsymbol{P}_{12} \\ \boldsymbol{P}_{21} & \boldsymbol{P}_{22}\end{bmatrix}\begin{bmatrix}\beta_1\mathrm{sgn}(\boldsymbol{e}_1) \\ \beta_2\mathrm{sgn}(\boldsymbol{e}_1) + \beta_3\int_0^t \mathrm{sgn}(\boldsymbol{e}_1)d\tau\end{bmatrix} \\
&= -2\boldsymbol{e}_1^T\boldsymbol{P}_{11}\beta_1\mathrm{sgn}(\boldsymbol{e}_1) - 2\boldsymbol{e}_2^T\boldsymbol{P}_{21}\beta_1 sgn(\boldsymbol{e}_1) - 2\boldsymbol{e}_1^T\boldsymbol{P}_{12}\beta_2\mathrm{sgn}(\boldsymbol{e}_1) \\
&\quad - 2\boldsymbol{e}_2^T\boldsymbol{P}_{22}\beta_2 sgn(\boldsymbol{e}_1) - 2\boldsymbol{e}_1^T\boldsymbol{P}_{12}\beta_3\int_0^t \mathrm{sgn}(\boldsymbol{e}_1)d\tau - 2\boldsymbol{e}_2^T\boldsymbol{P}_{22}\beta_3\int_0^t \mathrm{sgn}(\boldsymbol{e}_1)d\tau \\
&\le -2\boldsymbol{e}_2^T\boldsymbol{P}_{21}\beta_1\mathrm{sgn}(\boldsymbol{e}_1) - 2\boldsymbol{e}_1^T\boldsymbol{P}_{12}\beta_2\mathrm{sgn}(\boldsymbol{e}_1) - 2\boldsymbol{e}_2^T\boldsymbol{P}_{22}\beta_2\mathrm{sgn}(\boldsymbol{e}_1) \\
&\quad - 2\boldsymbol{e}_1^T\boldsymbol{P}_{12}\beta_3\int_0^t \mathrm{sgn}(\boldsymbol{e}_1)d\tau - 2\boldsymbol{e}_2^T\boldsymbol{P}_{22}\beta_3\int_0^t \mathrm{sgn}(\boldsymbol{e}_1)d\tau \\
&= \begin{bmatrix}\boldsymbol{e}_1^T & \boldsymbol{e}_2^T\end{bmatrix}\begin{bmatrix}-2\boldsymbol{P}_{12}\beta_2\mathrm{sgn}(\boldsymbol{e}_1) - 2\boldsymbol{P}_{12}\beta_3\int_0^t \mathrm{sgn}(\boldsymbol{e}_1)d\tau \\ -2\boldsymbol{P}_{21}\beta_1\mathrm{sgn}(\boldsymbol{e}_1) - 2\boldsymbol{P}_{22}\beta_2\mathrm{sgn}(\boldsymbol{e}_1) - 2\boldsymbol{e}_2^T\boldsymbol{P}_{22}\beta_3\int_0^t \mathrm{sgn}(\boldsymbol{e}_1)d\tau\end{bmatrix}
\end{aligned} \tag{24}$$

Define $\bar{\boldsymbol{B}}_1 = \begin{bmatrix}-2\boldsymbol{P}_{12}\beta_2\mathrm{sgn}(\boldsymbol{e}_1) - 2\boldsymbol{P}_{12}\beta_3\int_0^t \mathrm{sgn}(\boldsymbol{e}_1)d\tau \\ -2\boldsymbol{P}_{21}\beta_1\mathrm{sgn}(\boldsymbol{e}_1) - 2\boldsymbol{P}_{22}\beta_2\mathrm{sgn}(\boldsymbol{e}_1) - 2\boldsymbol{e}_2^T\boldsymbol{P}_{22}\beta_3\int_0^t \mathrm{sgn}(\boldsymbol{e}_1)d\tau\end{bmatrix}$, then $-2\boldsymbol{e}^T\boldsymbol{P}\bar{\boldsymbol{B}} \le \|\boldsymbol{B}_1\|\|\boldsymbol{e}\|$. To sum up the above, we can obtain the Equation (25)

$$\begin{aligned}
\dot{V}_0 &\le -\lambda_{\min}(\boldsymbol{\Lambda})\|\boldsymbol{e}\|^2 + \left(\frac{1}{\varepsilon}\|\boldsymbol{P}\|^2 + \varepsilon L_k\right)\|\boldsymbol{e}\|^2 + 2M_D\|\boldsymbol{P}\|\|\boldsymbol{e}\| + \|\boldsymbol{B}_1\|\|\boldsymbol{e}\| \\
&= \left(-\lambda_{\min}(\boldsymbol{\Lambda}) + \frac{1}{\varepsilon}\|\boldsymbol{P}\|^2 + \varepsilon L_k\right)\|\boldsymbol{e}\|^2 + (2M_D\|\boldsymbol{P}\| + \|\boldsymbol{B}_1\|)\|\boldsymbol{e}\|
\end{aligned} \tag{25}$$

According to Equation (25), Equation (26) can be obtained

$$\begin{aligned}
\dot{V}_0 &\le -\frac{\left(\lambda_{\min}(\boldsymbol{\Lambda}) - \frac{1}{\varepsilon}\|\boldsymbol{P}\|^2 - \varepsilon L_k\right)}{\lambda_{\max}(\boldsymbol{P})}V_0 + \frac{(2M_D\|\boldsymbol{P}\| + \|\boldsymbol{B}_1\|)}{\sqrt{\lambda_{\min}(\boldsymbol{P})}}V_0^{\frac{1}{2}} \\
&= -b_0V_0 + c_0V_0^{\frac{1}{2}}
\end{aligned} \tag{26}$$

where $b_0 = \frac{\left(\lambda_{\min}(\boldsymbol{\Lambda}) - \frac{1}{\varepsilon}\|\boldsymbol{P}\|^2 - \varepsilon L_k\right)}{\lambda_{\max}(\boldsymbol{P})}$, $c_0 = \frac{(2M_D\|\boldsymbol{P}\| + \|\boldsymbol{B}_1\|)}{\sqrt{\lambda_{\min}(\boldsymbol{P})}}$. According to Lemma 2, it can be known that the estimated error e converges in the region $Q_0 = \left\{\boldsymbol{e} : V_0 < \left(\frac{c_0}{\kappa_0}\right)^2\right\}$ in a finite time, where $\kappa_0 \in (0, b_0)$. The convergence time satisfies $T_0 \leq \frac{2}{b_0}\ln\left(\frac{b_0 V_0(\boldsymbol{e}(0)) - c_0}{b_0 c_0 / \kappa_0 - c_0}\right)$, and $\boldsymbol{e}$ is defined as $\boldsymbol{e}(0)$ at the time $t = 0$. When $V_0 < \left(\frac{c_0}{\kappa_0}\right)^2$, the upper bound of error $\|\boldsymbol{e}\| < \bar{\boldsymbol{e}} = \left(\frac{c_0}{\kappa_0}\right)/\sqrt{\lambda_{\min}(\boldsymbol{p})}$ can be obtained. On the basis of the error upper bound $\bar{\boldsymbol{e}}$, the finite time convergence properties of the error state vectors $\boldsymbol{e}_1$ and $\boldsymbol{e}_2$ are further proved.

For the error state vector $\boldsymbol{e}_1$, the Lyapunov function V_1 is designed as:

$$V_1 = \boldsymbol{e}_1^T \boldsymbol{P}_{11} \boldsymbol{e}_1 \tag{27}$$

Its time derivative is

$$\begin{aligned}
\dot{V}_1 &= \boldsymbol{e}_1^T \boldsymbol{P}_{11}\dot{\boldsymbol{e}}_1 + \dot{\boldsymbol{e}}_1^T \boldsymbol{P}_{11}\boldsymbol{e}_1 \\
&= -2l_1 \boldsymbol{e}_1^T \boldsymbol{P}_{11}\boldsymbol{e}_1 + 2\boldsymbol{e}_1^T \boldsymbol{P}_{11}\boldsymbol{e}_2 - 2\beta_1 \boldsymbol{e}_1^T \boldsymbol{P}_{11}\mathrm{sgn}(\boldsymbol{e}_1) + 2\boldsymbol{e}_1^T \boldsymbol{P}_{11}\boldsymbol{f}_{e1} \\
&\leq -2l_1\lambda_{\min}(\boldsymbol{P}_{11})\|\boldsymbol{e}_1\|^2 + 2\bar{\boldsymbol{e}}\|\boldsymbol{P}_{11}\|\|\boldsymbol{e}_1\| - 2\beta_1\lambda_{\min}(\boldsymbol{P}_{11})\|\boldsymbol{e}_1\| + \left(\frac{1}{\varepsilon_1}\|\boldsymbol{P}_{11}\|^2 + \varepsilon_1 L_k\right)\|\boldsymbol{e}_1\|^2 \\
&= -\left(2l_1\lambda_{\min}(\boldsymbol{P}_{11}) - \frac{1}{\varepsilon_1}\|\boldsymbol{P}_{11}\|^2 - \varepsilon_1 L_k\right)\|\boldsymbol{e}_1\|^2 - (2\beta_1\lambda_{\min}(\boldsymbol{P}_{11}) - 2\bar{\boldsymbol{e}}\|\boldsymbol{P}_{11}\|)\|\boldsymbol{e}_1\|
\end{aligned} \tag{28}$$

where according to Assumption 5, $L_k > 0$, $\varepsilon > 0$. Equation (28) can be rewritten as:

$$\begin{aligned}
\dot{V}_1 &\leq -\left(2l_1\lambda_{\min}(\boldsymbol{P}_{11}) - \frac{1}{\varepsilon_1}\|\boldsymbol{P}_{11}\|^2 - \varepsilon_1 L_k\right)\|\boldsymbol{e}_1\|^2 - (2\beta_1\lambda_{\min}(\boldsymbol{P}_{11}) - 2\bar{\boldsymbol{e}}\|\boldsymbol{P}_{11}\|)\|\boldsymbol{e}_1\| \\
&\leq -\frac{\left(2l_1\lambda_{\min}(\boldsymbol{P}_{11}) - \frac{1}{\varepsilon_1}\|\boldsymbol{P}_{11}\|^2 - \varepsilon_1 L_k\right)}{\lambda_{\max}(\boldsymbol{P}_{11})}V_1 - \frac{(2\beta_1\lambda_{\min}(\boldsymbol{P}_{11}) - 2\bar{\boldsymbol{e}}\|\boldsymbol{P}_{11}\|)}{\sqrt{\lambda_{\max}(\boldsymbol{P}_{11})}}V_1^{\frac{1}{2}} \\
&= -b_1 V_1 - c_1 V_1^{\frac{1}{2}}
\end{aligned} \tag{29}$$

where $b_1 = \frac{2l_1\lambda_{\min}(\boldsymbol{P}_{11}) - \frac{1}{\varepsilon_1}\|\boldsymbol{P}_{11}\|^2 - \varepsilon_1 L_k}{\lambda_{\max}(\boldsymbol{P}_{11})}$ and $c_1 = \frac{2\beta_1\lambda_{\min}(\boldsymbol{P}_{11}) - 2\bar{\boldsymbol{e}}\|\boldsymbol{P}_{11}\|}{\sqrt{\lambda_{\max}(\boldsymbol{P}_{11})}}$. By Lemma 3, the state error vector $\boldsymbol{e}_1$ converges to 0 in finite time. And the convergence time satisfies $T_1 \leq \frac{2}{b_1}\ln\left(1 + \frac{b_1}{c_1}V_1(\boldsymbol{e}_1(T_0))^{\frac{1}{2}}\right)$, where $\boldsymbol{e}_1$ at $t = T_0$ is defined as $\boldsymbol{e}_1(T_0)$. The above proves that ESHSMO can achieve finite time estimation of state vector $\boldsymbol{x}_1$ within $t = T_0 + T_1$.

According to the above, when $t \to (T_0 + T_1)$, then $\lim_{t\to(T_0+T_1)} \boldsymbol{e}_1 = \lim_{t\to(T_0+T_1)} \dot{\boldsymbol{e}}_1 = 0$. The equation of state of the estimated error can be rewritten as:

$$\begin{cases} \boldsymbol{e}_2 = \beta_1 \mathrm{sgn}(\boldsymbol{e_1}) \\ \dot{\boldsymbol{e}}_2 = -\beta_2 \mathrm{sgn}(\boldsymbol{e_1}) - \beta_3 \int_0^t \mathrm{sgn}(\boldsymbol{e}_1)d\tau + \dot{\boldsymbol{x}}_2 \end{cases} \tag{30}$$

Equation (30) is modified as follows:

$$\begin{cases} \dot{\boldsymbol{e}}_2 = -\mu_1 \boldsymbol{e}_2 + \dot{\boldsymbol{x}}_2 + \boldsymbol{e}_3 \\ \dot{\boldsymbol{e}}_3 = -\mu_2 \boldsymbol{e}_2 \end{cases} \tag{31}$$

where $\boldsymbol{e}_3 = -\beta_3\beta_1^{-1}\int_0^t \boldsymbol{e}_2 d\tau$, $\mu_1 = \beta_2\beta_1^{-1}$, $\mu_2 = \beta_3\beta_1^{-1}$. Let $\boldsymbol{e}' = \left[\boldsymbol{e}_2^T \ \boldsymbol{e}_3^T\right]^T$ and design the Lyapunov function as

$$V_2 = \boldsymbol{e}'^T \boldsymbol{P}_1' \boldsymbol{e}' \tag{32}$$

where $\boldsymbol{P}_1' = \begin{bmatrix} \left(\frac{1}{2}\mu_1^2 + \mu_2\right)\boldsymbol{I}_{6\times6} & -\frac{1}{2}\mu_1\boldsymbol{I}_{6\times6} \\ -\frac{1}{2}\mu_1\boldsymbol{I}_{6\times6} & \boldsymbol{I}_{6\times6} \end{bmatrix}$ and it is easy to know that $\boldsymbol{P}_1'$ is a positive definite matrix. Taking the time derivative of Lyapunov function V_2 and substituting it into Equation (31), we can obtain

$$\begin{aligned} \dot{V}_2 &= -\boldsymbol{e}'^T\boldsymbol{P}_2'\boldsymbol{e}' + \dot{\boldsymbol{x}}_2^T\boldsymbol{M}'\boldsymbol{e}' \\ &\leq -\frac{\lambda_{\min}(\boldsymbol{P}_2')}{\lambda_{\max}(\boldsymbol{P}_1')}V_2 + \frac{M_D\|\boldsymbol{M}'\|}{\sqrt{\lambda_{\min}(\boldsymbol{P}_1')}}V_2^{\frac{1}{2}} \\ &= -b_2V_2 + c_2V_2^{\frac{1}{2}} \end{aligned} \tag{33}$$

where $P_2' = \begin{bmatrix} \left(\mu_1\mu_2 + \mu_1^3\right)\boldsymbol{I}_{6\times6} & -\mu_1^2\boldsymbol{I}_{6\times6} \\ -\mu_1^2\boldsymbol{I}_{6\times6} & \mu_1\boldsymbol{I}_{6\times6} \end{bmatrix}$, $\boldsymbol{M}' = \begin{bmatrix} \left(2\mu_2 + \mu_2^2\right)\boldsymbol{I}_{6\times6} & -\mu_1\boldsymbol{I}_{6\times6} \end{bmatrix}$, $b_2 = \frac{\lambda_{\min}(\boldsymbol{P}_2')}{\lambda_{\max}(\boldsymbol{P}_1')}$, $c_2 = \frac{M_D\|\boldsymbol{M}'\|}{\sqrt{\lambda_{\min}(\boldsymbol{P}_1')}}$ and it is easy to know that $\boldsymbol{P}_2'$ is a positive definite matrix. By Lemma 2, it can be known that $\boldsymbol{e}'$ converges to region $Q_2 = \left\{\boldsymbol{e}' : V_2 < \left(\frac{c_2}{\kappa_2}\right)^2\right\}$ in finite time, where $\kappa_2 \in (0, b_2)$. The convergence time satisfies $T_2 \leq \frac{2}{b_2}\ln\left(\frac{b_2V_2(\boldsymbol{e}'(T_0+T_1))-c_2}{b_2c_2/\kappa_2-c_2}\right)$, $\boldsymbol{e}'$ at time $t = T_0 + T_1$ is defined as $\boldsymbol{e}'(T_0 + T_1)$. When $V_2 < \left(\frac{c_2}{\kappa_2}\right)^2$, the error upper bound $\|\boldsymbol{e}_2\| < \|\boldsymbol{e}'\| = \left(\frac{c_2}{\kappa_2}\right)/\sqrt{\lambda_{\min}(\boldsymbol{P}_1')}$ can be obtained. The above proves that ESHSMO can realize the finite-time estimation of the state vector $\boldsymbol{x}_2$ within the time $t = T_0 + T_1 + T_2$; that is, the estimation errors of the current velocity disturbance $\boldsymbol{v}_f$ and the lumped disturbance $\boldsymbol{\tau}_D$ converge to a certain region. The above completes the proof of Theorem 1. □

4. Fast Finite-Time Super-Twisting Sliding Mode Control

In this section, a fast finite-time super-twisting sliding mode control approach is designed on the basis of disturbances and model uncertainties observation from the ESHSMO. The FSTSMC approach ensures that the UUV can track the target trajectory in a fast manner and with a high control precision. Meanwhile, the stability analysis of the FSTSMC is also being conducted.

4.1. Design of FSTSMC

Define the UUV tracking error vector as:

$$\boldsymbol{e}_\eta = \boldsymbol{\eta} - \boldsymbol{\eta}_d \tag{34}$$

where $\boldsymbol{\eta}_d$ is the target trajectory vector. The derivative estimate of the tracking error vector is defined as:

$$\hat{\dot{\boldsymbol{e}}}_\eta = \hat{\dot{\boldsymbol{\eta}}} - \dot{\boldsymbol{\eta}}_d = \boldsymbol{J}(\eta)\boldsymbol{v}_r + \hat{\boldsymbol{v}}_f - \dot{\boldsymbol{\eta}}_d \tag{35}$$

Design sliding mode vector s as:

$$\boldsymbol{s} = \hat{\dot{\boldsymbol{e}}}_\eta + \boldsymbol{C}\boldsymbol{e}_\eta \tag{36}$$

where $\boldsymbol{C}$ is the sliding mode surface parameter matrix, which is the positive definite diagonal matrix. Substituting Equation (35) into Equation (36), the following can be obtained

$$\boldsymbol{s} = \boldsymbol{J}(\eta)\boldsymbol{v}_r + \hat{\boldsymbol{v}}_f - \dot{\boldsymbol{\eta}}_d + \boldsymbol{C}(\boldsymbol{\eta} - \boldsymbol{\eta}_d) \tag{37}$$

Take the time derivative of sliding mode vector s as:

$$\dot{\boldsymbol{s}} = \dot{\boldsymbol{J}}(\eta)\boldsymbol{v}_r + \boldsymbol{J}(\eta)\dot{\boldsymbol{v}}_r + \dot{\hat{\boldsymbol{v}}}_f - \ddot{\boldsymbol{\eta}}_d + \boldsymbol{C}\dot{\boldsymbol{\eta}} - \boldsymbol{C}\dot{\boldsymbol{\eta}}_d \tag{38}$$

Substitute Equation (9) into Equation (38) to obtain

$$\dot{\boldsymbol{s}} = \dot{\boldsymbol{J}}(\eta)\boldsymbol{v}_r + \boldsymbol{J}(\eta)\left(-\boldsymbol{M}_0^{-1}\boldsymbol{f}(\boldsymbol{v}_r,\boldsymbol{\eta}) + \boldsymbol{M}_0^{-1}\boldsymbol{\tau}_T + \boldsymbol{\tau}_{MD}\right) + \dot{\hat{\boldsymbol{v}}}_f - \ddot{\boldsymbol{\eta}}_{\boldsymbol{d}} + \boldsymbol{C}\left(\boldsymbol{J}(\eta)\boldsymbol{v}_r + \boldsymbol{v}_f\right) - \boldsymbol{C}\dot{\boldsymbol{\eta}}_{\boldsymbol{d}} \tag{39}$$

In order to achieve rapid convergence of sliding mode variables and weaken the chattering phenomenon, the following smooth fast super-twisting sliding mode reaching law is designed:

$$\dot{\boldsymbol{s}} = -\left(\boldsymbol{K}_1\boldsymbol{s}^{\frac{m-1}{m}} + \boldsymbol{K}_2\boldsymbol{s}\right) - \int_0^t \left(\boldsymbol{K}_3\boldsymbol{s}^{\frac{m-2}{m}} + \boldsymbol{K}_4\boldsymbol{s}\right)d\tau \tag{40}$$

Substituting Equation (39) into Equation (40), the fast finite-time super-twisting sliding mode control law based on ESHSMO is designed as:

$$\begin{aligned}\boldsymbol{\tau}_T = {} & \boldsymbol{f}(\boldsymbol{v}_r,\boldsymbol{\eta}) - \boldsymbol{M}_0\hat{\boldsymbol{\tau}}_{MD} - \boldsymbol{M}_0\boldsymbol{J}(\boldsymbol{\eta})^{-1}\left[\dot{\boldsymbol{J}}(\boldsymbol{\eta})\boldsymbol{v}_r + \dot{\hat{\boldsymbol{v}}}_f - \ddot{\boldsymbol{\eta}}_d\right] - \boldsymbol{M}_0\boldsymbol{J}(\boldsymbol{\eta})^{-1}\boldsymbol{C}\left[\boldsymbol{J}(\boldsymbol{\eta})\boldsymbol{v}_r - \dot{\boldsymbol{\eta}}_d + \hat{\boldsymbol{v}}_f\right] \\ & - \boldsymbol{M}_0\boldsymbol{J}(\boldsymbol{\eta})^{-1}\left[\boldsymbol{K}_1\lceil\boldsymbol{s}\rfloor^{\frac{m-1}{m}} + \boldsymbol{K}_2\boldsymbol{s}\right] - \boldsymbol{M}_0\boldsymbol{J}(\boldsymbol{\eta})^{-1}\int_0^t\left[\boldsymbol{K}_3\lceil\boldsymbol{s}\rfloor^{\frac{m-2}{m}} + \boldsymbol{K}_4\boldsymbol{s}\right]d\tau\end{aligned} \tag{41}$$

where $\boldsymbol{K}_1$, $\boldsymbol{K}_2$ are the sliding mode approach matrix, and $\boldsymbol{K}_3$, $\boldsymbol{K}_4$ are the higher-order sliding mode approach matrix. They are all the positive definite diagonal matrix. To satisfy the following proof of stability, $-\left[\frac{m^3K_{3i}}{m-1} + (4m^2-4m+1)K_{1i}^2\right] + m^2K_{3i}K_{4i}\,K_{2i}^2 > 0, i = 1,\ldots,6, m > 2$.

Since Equation (41) does not directly contain a sign function alone, the control law is continuous, which effectively weakens chattering of the control output and ensures the robustness of the system. Meanwhile, when the sliding mode variable is far away from the sliding mode surface, the convergence rate mainly depends on the linear term in Equation (41); when the sliding mode variable is close to the sliding mode surface, the convergence rate mainly depends on the nonlinear term in Equation (41). Therefore, the control law has a fast convergence rate regardless of whether the sliding mode variable is far away from the sliding mode surface.

4.2. Stability Analysis of FSTSMC

Theorem 2. *For UUV with unknown ocean current and lumped disturbance described by Equations (6) and (9), the trajectory tracking error will converge in finite time under the ESHSMO based on Equation (12) and the FSTSMC based on Equation (41).*

Proof. By substituting the fast finite-time super-twisting sliding mode control law (41) into Equation (39),

$$\dot{\boldsymbol{s}} = \boldsymbol{J}(\eta)(\boldsymbol{\tau}_{MD} - \hat{\boldsymbol{\tau}}_{MD}) + \boldsymbol{C}\left(\boldsymbol{v}_f - \hat{\boldsymbol{v}}_f\right) - \left(\boldsymbol{K}_1\lceil\boldsymbol{s}\rfloor^{\frac{m-1}{m}} + \boldsymbol{K}_2\boldsymbol{s}\right) - \int_0^t\left(\boldsymbol{K}_3\lceil\boldsymbol{s}\rfloor^{\frac{m-2}{m}} + \boldsymbol{K}_4\boldsymbol{s}\right)d\tau \tag{42}$$

Let $\boldsymbol{\Gamma} = \boldsymbol{J}(\eta)(\boldsymbol{\tau}_{MD} - \hat{\boldsymbol{\tau}}_{MD}) + \boldsymbol{C}\left(\boldsymbol{v}_f - \hat{\boldsymbol{v}}_f\right)$, according to the ESHSMO observation error convergence property, it can be known that $|\Gamma_i|_{\max} = \max\{|\Gamma_1|,\ldots,|\Gamma_6|\} \le \Upsilon$, where Υ is a specific positive real number. Equation (42) can be written as

$$\dot{\boldsymbol{s}} = -\left(\boldsymbol{K}_1\lceil\boldsymbol{s}\rfloor^{\frac{m-1}{m}} + K_2s\right) - \int_0^t\left(\boldsymbol{K}_3\lceil\boldsymbol{s}\rfloor^{\frac{m-2}{m}} + \boldsymbol{K}_4\boldsymbol{s}\right)d\tau + \boldsymbol{\Gamma} \tag{43}$$

Equation (43) can be modified as the following second-order nonlinear system:

$$\begin{cases}\dot{\boldsymbol{s}} = -\boldsymbol{K}_1\lceil\boldsymbol{s}\rfloor^{\frac{m-1}{m}} - \boldsymbol{K}_2\boldsymbol{s} + \boldsymbol{z} \\ \dot{\boldsymbol{z}} = -\boldsymbol{K}_3\lceil\boldsymbol{s}\rfloor^{\frac{m-2}{m}} - \boldsymbol{K}_4\boldsymbol{s} + \dot{\boldsymbol{\Gamma}}\end{cases} \tag{44}$$

Let us define the Lyapunov function as

$$V = \boldsymbol{\xi}^T\prod\boldsymbol{\xi} \tag{45}$$

where $\xi = \left[\left(\lceil s \rfloor^{\frac{m-1}{m}}\right)^T, s^T, z^T\right]^T$, $\prod = \frac{1}{2}\begin{bmatrix} \frac{2m}{m-1}K_3 + K_1^2 & K_1K_2 & -K_1 \\ K_1K_2 & 2K_4 + K_2^2 & -K_2 \\ -K_1 & -K_2 & 2I_{6\times 6} \end{bmatrix}$, and $\prod$ is a positive definite matrix. Taking the time derivative of the Lyapunov function (45), we can obtain

$$\dot{V} = -\xi^T \Omega \prod\nolimits_1 \xi - \xi^T \prod\nolimits_2 \xi + \Gamma^T \zeta \xi \tag{46}$$

where $\Omega = \begin{bmatrix} |s|^{-\frac{1}{m}} & & \\ & |s|^{-\frac{1}{m}} & \\ & & |s|^{-\frac{1}{m}} \end{bmatrix}$, $\prod_1 = \frac{1}{m}\begin{bmatrix} mK_1K_3 + (m-1)K_1^3 & 0_{6\times 6} & -(m-1)K_1^2 \\ 0_{6\times 6} & mK_1K_4 + (3m-1)K_1K_2^2 & -(2m-1)K_1K_2 \\ -(m-1)K_1^2 & -(2m-1)K_1K_2 & (m-1)K_1 \end{bmatrix}$, $\zeta = \begin{bmatrix} -K_1 & -K_2 & 2I_{6\times 6} \end{bmatrix}$, $\prod_2 = \begin{bmatrix} K_2K_3 + \frac{3m-2}{m}K_1^2K_2 & 0_{6\times 6} & 0_{6\times 6} \\ 0_{6\times 6} & K_2K_4 + K_2^3 & -K_2^2 \\ 0_{6\times 6} & -K_2^2 & K_2 \end{bmatrix}$. Since $m^2K_{3i}K_{4i} - \left[\frac{m^3K_{3i}}{m-1} + \left(4m^2 - 4m + 1\right)K_{1i}^2\right]K_{2i}^2 > 0$, $i = 1, \ldots, 6$ is established, it is easy to obtain $\prod_1, \prod_2$ as a positive definite matrix. It can be deduced from the above

$$\dot{V} \le -\lambda_{\min}(\Omega)\lambda_{\min}\left(\prod_1\right)\|\xi\|^2 - \lambda_{\min}\left(\prod_2\right)\|\xi\|^2 + \Upsilon\|\zeta\|\|\xi\| \tag{47}$$

From Equation (45), it can be known that

$$\lambda_{\min}\left(\prod\right)\|\xi\|^2 \le V \le \lambda_{max}\left(\prod\right)\|\xi\|^2 \tag{48}$$

then

$$\|\xi\| \le V^{\frac{1}{2}} \Big/ \lambda_{\min}\left(\prod\right)^{\frac{1}{2}} \tag{49}$$

It can also be deduced that

$$\|\xi\| \ge \left\|\lceil s \rfloor^{\frac{m-1}{m}}\right\| = \left\||s|^{\frac{m-1}{m}}\right\| \ge \sqrt{6}[\lambda_{\min}(\Omega)]^{-(m-1)} \tag{50}$$

Combining Equations (49) and (50), it can be deduced that

$$\lambda_{\min}(\Omega) \ge \sqrt{6}^{\frac{1}{m-1}}\left[\lambda_{\min}\left(\prod\right)^{\frac{1}{2m-2}} \Big/ V^{\frac{1}{2m-2}}\right] \tag{51}$$

Substitute Equation (51) into (47) to obtain

$$\dot{V} \le -\sqrt{6}^{\frac{1}{m-1}}\left[\lambda_{\min}\left(\prod\right)^{\frac{1}{2m-2}} \Big/ V^{\frac{1}{2m-2}}\right]\lambda_{\min}\left(\prod_1\right)\|\xi\|^2 - \lambda_{\min}\left(\prod_2\right)\|\xi\|^2 + \Upsilon\|\zeta\|\|\xi\| \tag{52}$$

Referring to Lemma 4, Equation (52) can be rewritten as

$$\begin{aligned} V &\le -\sqrt{6}^{\frac{1}{m-1}}\frac{\lambda_{\min}(\prod)^{\frac{1}{2m-2}}\lambda_{\min}(\prod_1)}{\lambda_{\max}(\prod)}V^{\frac{2m-3}{2m-2}} - \frac{\lambda_{\min}(\prod_2)}{\lambda_{\max}(\prod)}V + \frac{\Upsilon\|\zeta\|}{\lambda_{\min}(\prod)^{\frac{1}{2}}}V^{\frac{1}{2}} \\ &= -b_3V^{a_3} - c_3V + d_3V^{\frac{1}{2}} \end{aligned} \tag{53}$$

where $a_3 = \frac{2m-3}{2m-2}$, $b_3 = \sqrt{6}^{\frac{1}{m-1}}\frac{\lambda_{\min}(\prod)^{\frac{1}{2m-2}}\lambda_{\min}(\prod_1)}{\lambda_{\max}(\prod)}$, $c_3 = \frac{\lambda_{\min}(\prod_2)}{\lambda_{\max}(\prod)}$, $d_3 = \frac{\Upsilon\|\zeta\|}{\lambda_{\min}(\prod)^{\frac{1}{2}}}$. According to Lemma 4, when $b_3, c_3, d_3 > 0$, $0 < a_3 < 0.5$, it can be known that e_η converges to the region $\Omega_3 = \left\{e_\eta : \kappa_{31}V^{a_3-\frac{1}{2}} + \kappa_{32}V^{\frac{1}{2}} < d_3\right\}$ in finite time, where $\kappa_{31} \in (0, b_3)$ and $\kappa_{32} \in (0, c_3)$. Then, the convergence time of the system satisfies $T_3 \le \frac{1}{(c_3-\kappa_{32})(1-a_3)}\ln\left(\frac{(c_3-\kappa_{32})V(\xi(0))^{1-a_3}+b_3-\kappa_{31}}{b_3-\kappa_{31}}\right)$, and ξ at time $t = 0$ is defined as $\xi(0)$. It is proved that the control scheme proposed in this paper can achieve fast finite time tracking of the UUV target trajectory with unknown ocean currents and external disturbances. Theorem 2 is proved. □

5. Numerical Simulation and Experimental Verification

In this section, the UUV platform is first introduced in Section 5.1. In Sections 5.2 and 5.3, the numerical simulation and the experiment in a water pool were conducted to compare and analyze the performance of the proposed trajectory tracking control scheme.

5.1. Uuv Platform

The UUV is 3100 mm × 2000 mm × 1800 mm in size and weighs 4187.5 kg. The dynamic parameters of the UUV are as follows: the center of gravity coordinates $\boldsymbol{r}_G = [0,0,0]^T$, the center of buoyancy coordinates $\boldsymbol{r}_B = [0,0,-0.493]^T$, the moment of inertia matrix $\boldsymbol{I} = diag(2038, 3587, 3587)$, the additional mass matrix $\boldsymbol{M}_{AM} = -diag(3261.35, 4664.31, 7471.75, 1664.00, 4118.17, 3708.41)$, the linear term of damping matrix $\boldsymbol{D}_L = -diag(3610.00, 2462.99, 4566.59, 9810.00, 5220.90, 5841.54)$ and the nonlinear term of damping matrix $\boldsymbol{D}_N = -diag(952.00|u|, 2442.78|v|, 530.46|w|, 890.00|p|, 1876.00|q|, 2085.52|r|)$. The structure of the UUV is shown in Figure 2. It is equipped with four horizontal thrusters and four vertical thrusters; the spatial distribution is shown in Table 1. The distribution matrix is

$$\boldsymbol{B} = \begin{bmatrix} c(35^\circ) & c(-35^\circ) & c(145^\circ) \\ s(35^\circ) & s(-35^\circ) & s(145^\circ) \\ 0 & 0 & 0 \\ 0.185s(35^\circ) & -0.185s(-35^\circ) & 0.185s(145^\circ) \\ -0.185c(35^\circ) & -0.185c(-35^\circ) & 0.185c(145^\circ) \\ 0.960c(35^\circ) + 1.250s(35^\circ) & -(0.960c(-35^\circ) + 1.250s(-35^\circ)) & -(0.960c(145^\circ) + 1.250s(145^\circ)) \\ c(215^\circ) & 0 & 0 \\ s(215^\circ) & -s(10^\circ) & -s(-10^\circ) \\ 0 & c(10^\circ) & c(-10^\circ) \\ -0.185s(215^\circ) & -(0.875s(10^\circ) + 0.678c(10^\circ)) & 0.875s(-10^\circ) + 0.678c(-10^\circ) \\ 0.185c(215^\circ) & -0.925c(10^\circ) & -0.925c(-10^\circ) \\ 0.960c(215^\circ) + 1.250s(215^\circ) & -0.925s(10^\circ) & 0.925s(-10^\circ) \end{bmatrix}$$

$$\begin{bmatrix} 0 & 0 \\ -s(10^\circ) & -s(-10^\circ) \\ c(10^\circ) & c(-10^\circ) \\ -(0.875s(10^\circ) + 0.678c(10^\circ)) & 0.875s(-10^\circ) + 0.678c(-10^\circ) \\ 0.925c(10^\circ) & 0.925c(-10^\circ) \\ 0.925s(10^\circ) & -0.925s(-10^\circ) \end{bmatrix}.$$

Among them, s represents sin and c represents cos. It is worth noting that the thrust output range of the thrusters equipped with the UUV is $[-3600\,\mathrm{N}, 3600\,\mathrm{N}]$. The influence of the saturation nonlinear characteristics has been considered in the simulation.

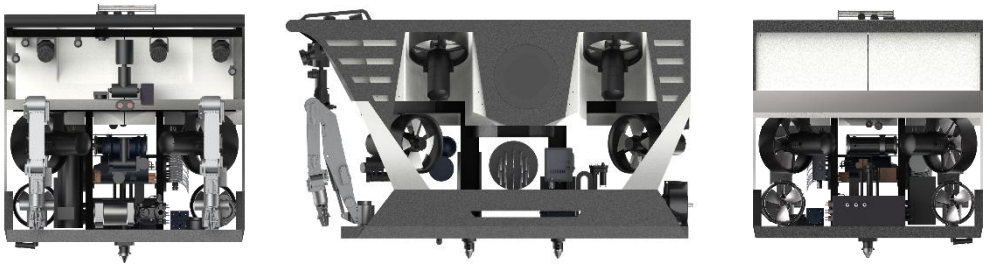


Figure 2. The structure of the platform. Front view (left), left view (middle) and rear view (right).

Table 1. Spatial distribution of the UUV thrusters.

Serial Number of the Thrusters		Description	x	y	z	Angle of Installation
Horizontal thrusters	1	Bow left horizontal thruster	1.250	−0.960	−0.185	35° to axis Ox
	2	Bow right horizontal thruster	1.250	0.960	−0.185	−35° to axis Ox
	3	Stern left horizontal thruster	−1.250	−0.960	−0.185	145° to axis Ox
	4	Stern right horizontal thruster	−1.250	0.960	−0.185	215° to axis Ox
Vertical thrusters	5	Bow left vertical thruster	0.925	−0.678	−0.875	10° to axis Oz
	6	Bow right vertical thruster	0.925	0.678	−0.875	−10° to axis Oz
	7	Stern left vertical thruster	−0.925	-0.678	−0.875	10° to axis Oz
	8	Stern right vertical thruster	−0.925	0.678	−0.875	−10° to axis Oz

5.2. Numerical Simulation

Numerical Simulation includes scenario 1 and scenario 2. Simulation scenario 1 is to verify the performance of FSTSMC. The tracking trajectory in numerical simulation is set as:

$$\begin{cases} x_d = 5\sin(0.05t) \\ y_d = 5\cos(0.05t) \\ z_d = 0.05t \\ \phi_d = 0 \\ \theta_d = 0 \\ \psi_d = 0 \end{cases} \tag{54}$$

The initial position and velocity of UUV are set as $\boldsymbol{\eta}(0) = [-5, 8, 0.5, -2, 2, 2]$, $\boldsymbol{v}(0) = [0, 0, 0, 0, 0, 0]$. The tuning parameters in FSTSMC include m, $\boldsymbol{C}$, $\boldsymbol{K}_1$, $\boldsymbol{K}_2$, $\boldsymbol{K}_3$ and $\boldsymbol{K}_4$. Here, m is the exponential power parameter vector of the sliding mode variable, which mainly affects the approaching speed of the sliding mode variable which is close to the sliding mode surface. $\boldsymbol{C}$ is the sliding mode surface parameter matrix, which mainly affects the convergence speed of sliding mode variables on the sliding mode surface. The larger the above two parameters, the faster the error convergence speed, and the chattering phenomenon may be more obvious. $\boldsymbol{K}_1$ and $\boldsymbol{K}_2$ are the sliding mode approach matrix values, which mainly affect the time and speed of sliding mode variables approaching and moving to the sliding mode surface, and they determine the chattering of the control output. The larger the parameter, the stronger the system robustness; however, the more serious the chattering phenomenon may be. $\boldsymbol{K}_3$ and $\boldsymbol{K}_4$ represent the higher-order sliding mode approach matrix. It can not only ensure the high precision and strong robustness of sliding mode control but also attenuate the chattering phenomenon. But it may cause a delay to the system. The parameter tuning procedure is as follows. First of all, $\boldsymbol{C}$ is usually set as the unit array, and m is set according to the control performance requirements. After that, $\boldsymbol{K}_1$ and $\boldsymbol{K}_2$ are tuned so that the sliding mode variables can quickly move to the sliding mode surface and eventually converge to 0. Finally, introduce $\boldsymbol{K}_3$ and $\boldsymbol{K}_4$, and appropriately reduce the elements in $\boldsymbol{K}_1$ and $\boldsymbol{K}_2$. This can not only obtain good control performance but also attenuate the chattering phenomenon. After comprehensive consideration and tuning, FSTSMC control parameters are tuned as: $m = 3$, $\boldsymbol{C} = diag(1, 1, 1, 1, 1, 1)$, $\boldsymbol{K}_1 = diag(0.5, 0.5, 0.5, 0.5, 0.5, 0.5)$, $\boldsymbol{K}_2 = diag(0.01, 0.01, 0.01, 100, 100, 50)$, $\boldsymbol{K}_3 = diag(0.001, 0.001, 0.001, 0.001, 0.001, 0.001)$, $\boldsymbol{K}_4 = diag(0.001, 0.001, 0.001, 0.001, 0.001, 0.001)$.

To further illustrate the trajectory tracking performance of FSTSMC, it will be compared with the super-twisting integral sliding mode control (STISMC) proposed by Manzanilla [34]. The simulation results of UUV trajectory tracking based on FSTSMC and STISMC are shown in Figures 3–5. Meanwhile, the root mean square error, convergence

time and steady-state error performance indicators are introduced to quantitatively analyze the trajectory tracking performance, as shown in Table 2.

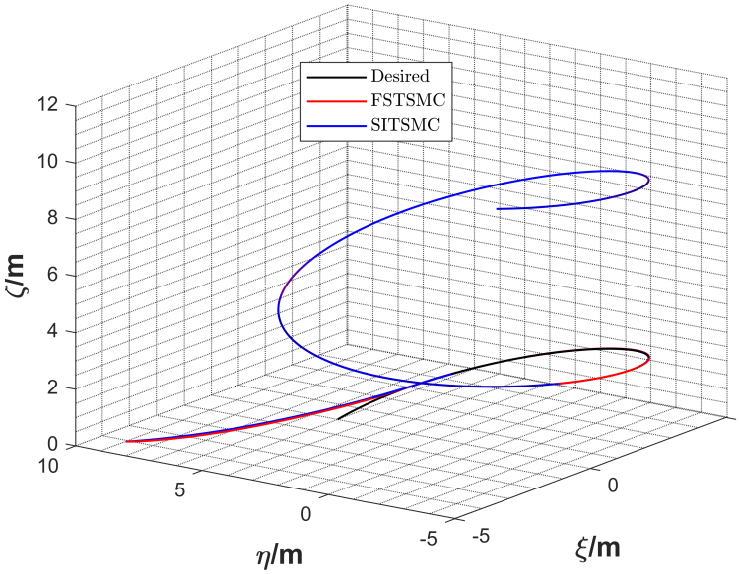


Figure 3. Trajectory tracking results of FSTSMC and SITSMC. Desired trajectory (black line), FSTSMC trajectory (red line) and SITSMC trajectory (blue line).

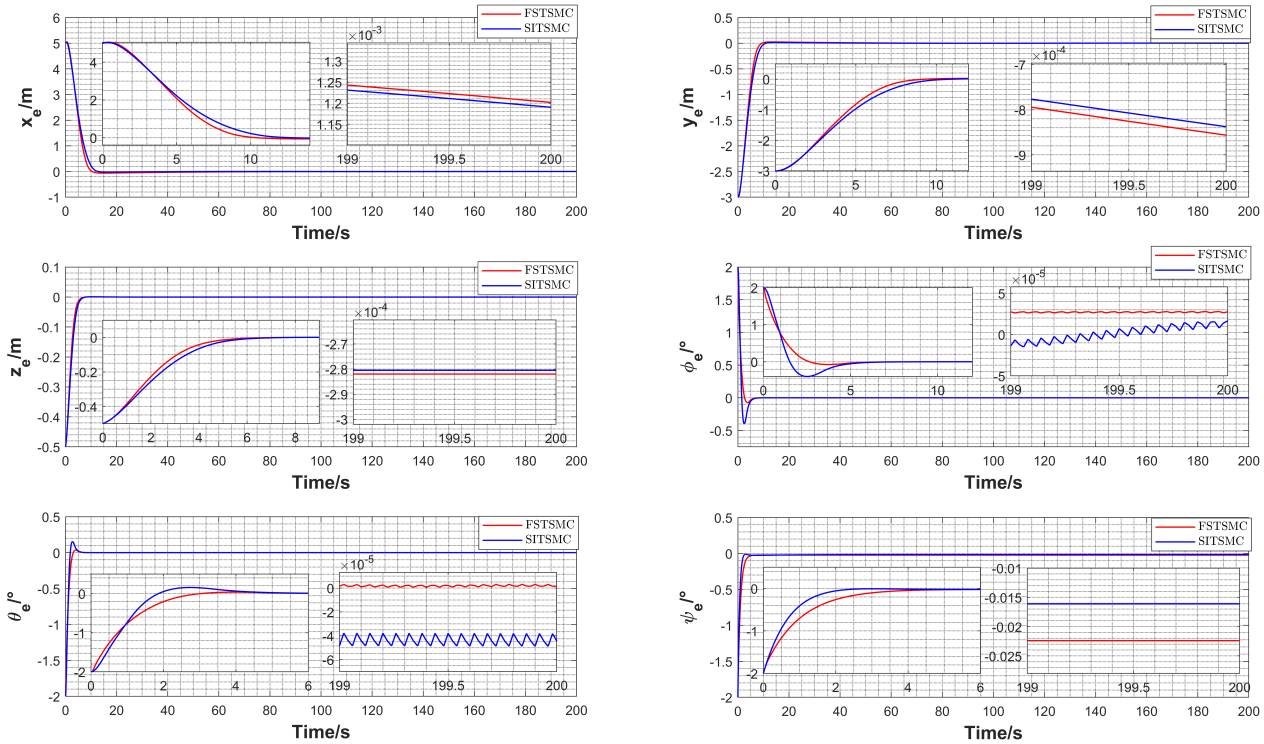


Figure 4. Trajectory tracking error under FSTSMC and SITSMC. FSTSMC trajectory error (red line) and SITSMC trajectory error (blue line).

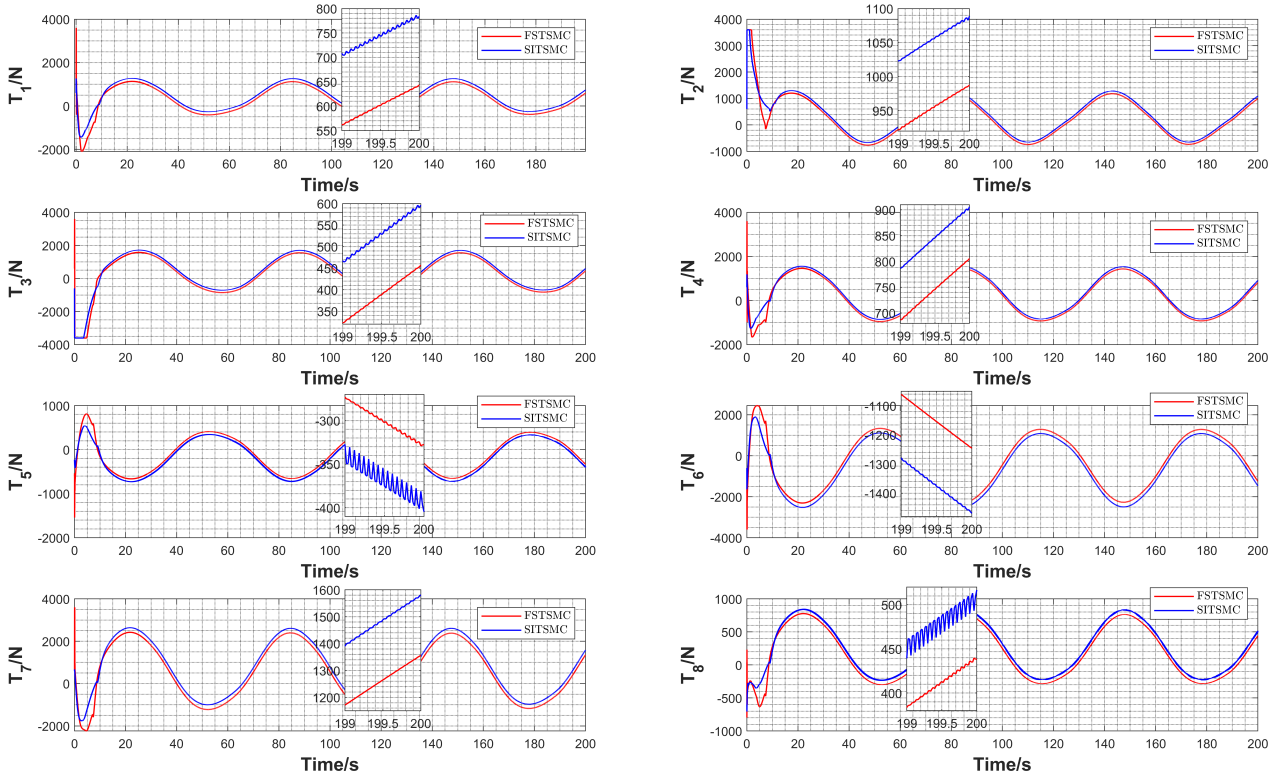


Figure 5. Thruster thrust under FSTSMC and SITSMC. FSTSMC thrust (red line) and SITSMC thrust (blue line).

Table 2. Quantitative comparison of FSTSMC and SITSMC trajectory tracking simulation results.

Performance Indicators	Control Approach	x	y	z	ϕ	θ	ψ
Root mean square error	FSTSMC	**0.6570**	**0.3468**	**0.0411**	**0.1013**	**0.1034**	0.1001
	STISMC	0.6633	0.3542	0.0429	0.1143	0.1082	**0.0840**
Convergence time	FSTSMC	**8.54**	**7.36**	**4.52**	**2.20**	**2.38**	3.06
	STISMC	9.86	8.34	5.00	4.36	3.54	**1.74**
Steady-state error	FSTSMC	0.0012	**−0.00084**	−0.00028	2.7×10^{-5}	$\mathbf{1.6 \times 10^{-6}}$	−0.022
	STISMC	0.0012	-0.00086	−0.00028	$\mathbf{1.7 \times 10^{-5}}$	-4.5×10^{-5}	**−0.016**

According to Figure 3, both FSTSMC and STISMC can accomplish the 3D trajectory tracking task. As can be seen from Figure 4, the position error tracking based on FSTSMC converges faster, the angular error converges more smoothly, and the overshoot is avoided. This is due to the addition of fast term $-\boldsymbol{M}_0\boldsymbol{J}(\boldsymbol{\eta})^{-1}\left[\boldsymbol{K}_2\boldsymbol{s} + \int_0^t \boldsymbol{K}_4\boldsymbol{s}d\tau\right]$ in FSTSMC, which accelerates the convergence speed of sliding mode variables when they are far away from the sliding mode surface. At the same time, this also makes the process of sliding mode variables approaching and crossing the sliding mode surface smoother. In addition, FSTSMC has obtained better performance on attenuating chattering compared with STISMC, as shown in Figure 5. It also demonstrates that the sliding mode variables in FSTSMC have a smaller oscillation amplitude when moving along the sliding surface. It can be found from Table 2 that FSTSMC has smaller root mean square error and shorter convergence time in degree of freedom x, y, z, ϕ, θ, while STISMC has smaller root mean square error and shorter convergence time in degree of freedom ψ, which is consistent with the results described in Figure 4. The steady-state errors obtained by the two approaches have little difference and are sufficient to meet the requirements of general trajectory tracking tasks. According to the above simulation results, it can be seen that both FSTSMC and STISMC

can achieve good trajectory tracking, while FSTSMC contributes better overall performance, and STISMC performs better in directional control. Moreover, FSTSMC has advantages in weakening chattering and fast convergence.

In order to further verify the robustness of the FSTSMC method to measurement noise, Gaussian distribution noise with standard deviation of 0.01 m, 0.1°, 0.01 m/s and 0.1°/s is added to position measurement and velocity measurement, respectively. The trajectory tracking simulation with measurement noise is carried out.

As can be seen from Figure 6, FSTSMC shows good robustness and control performance for measuring noise. Compared with the control effect of no measurement error, FSTSMC keeps the trajectory tracking error in a small range and successfully executes the trajectory tracking task.

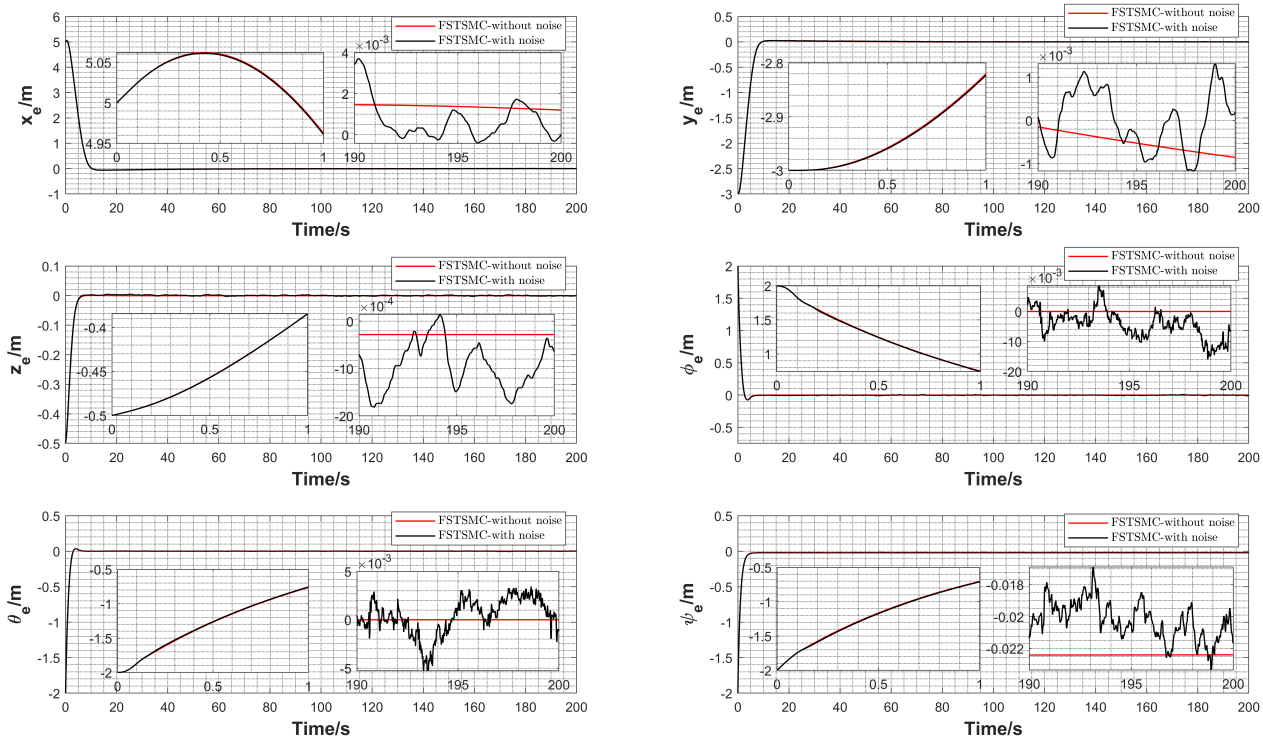


Figure 6. Trajectory tracking error under FSTSMC without noise and FSTSMC with noise. The FSTSMC without noise trajectory error (red line) and FSTSMC with noise trajectory error (black line).

In order to verify the performance of the ESHSMO proposed in this paper on the external current disturbances and model uncertainties, as well as the control performance of ESHSMO-FSTSMC, the ocean current velocity $\boldsymbol{v}_f$ and the lumped disturbance $\boldsymbol{\tau}_D$ in simulation scenario 2 are set to $\boldsymbol{v}_f = \left[0.3\sin(0.05t + \pi/3), 0.3\sin(0.05t + \pi/3), 0, 0, 0, 0\right]^T$,

$$\boldsymbol{\tau}_D = \begin{bmatrix} 1000\cos(0.05t + \pi/3)\sin(0.05t) \\ 1000\cos(0.05t + \pi/4)\cos(0.05t) \\ 1000\cos(0.05t + \pi/6)\sin(0.05t + \pi/4) \\ 1000\cos(0.05t + \pi/3)\cos(0.05t + \pi/10) \\ 1000\sin(0.05t)\sin(0.05t + \pi/3) \\ 1000\sin(0.05t + \pi/3)\cos(0.05t) \end{bmatrix}$$

, respectively. Meanwhile, UUV initial conditions and control approach parameters remain unchanged from simulation scenario 1. The tuning parameters in ESHSMO include l_1, l_2, β_1, β_2, β_3. l_1 and l_2 are the observation error feedback gain parameters, which determine the convergence of observation error. The larger the parameter, the faster the convergence speed. But it is easy to introduce high-frequency interference and even destroy the stability of the system. β_1, β_2, and β_3 are observer higher-order sliding mode parameters, which can accelerate the convergence of observation errors and improve the robustness of the observer. The parameter tuning

procedure is as follows. Firstly, l_1 and l_2 are set to relatively large values so that the observation error can quickly and stably converge. After that, introducing β_1, β_2, and β_3 and appropriately reducing l_1 and l_2 ensures good observation performance. After comprehensive consideration and tuning, ESHSMO parameters are set as: $l_1 = 10$, $l_2 = 1$, $\beta_1 = 2$, $\beta_2 = 20$, $\beta_3 = 10$.

The fast finite-time extended state observer (FFTESO) proposed by Ali [1] is introduced and combined with FSTSMC with the same parameters to compare and verify the observation performance of ESHSMO. Simulation results of trajectory tracking of UUV based on ESHSMO-FSTSMC and FFTESO-FSTSMC are shown in Figures 7–11.

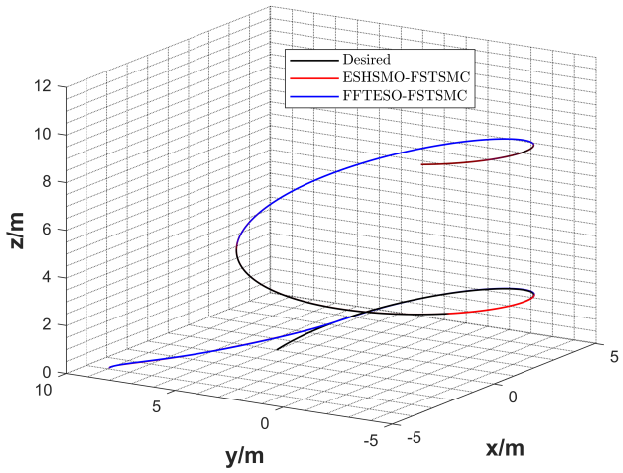


Figure 7. Trajectory tracking results of ESHSMO-FSTSMC and FFTESO-FSTSMC. Desired trajectory (black line), ESHSMO-FSTSMC trajectory (red line) and ESHSMO-SITSMC trajectory (blue line).

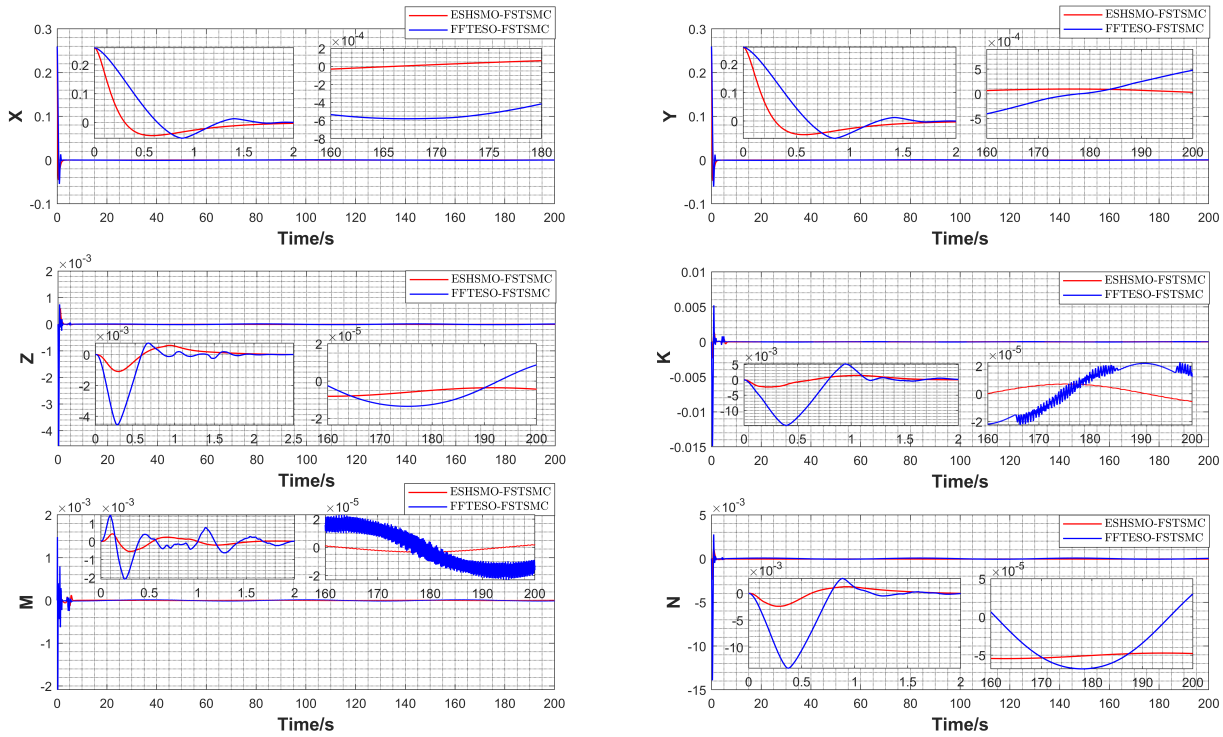


Figure 8. Observation error of ocean current velocity under ESHSMO-FSTSMC and FFTESO-FSTSMC. ESHSMO-FSTSMC observation error of ocean current velocity (red line) and FFTESO-FSTSMC observation error of ocean current velocity (blue line). Moreover, note that the six degrees of freedom for surge, sway, heave, roll, pitch, and yaw are represented by the letters X, Y, Z, K, M, and N, respectively.

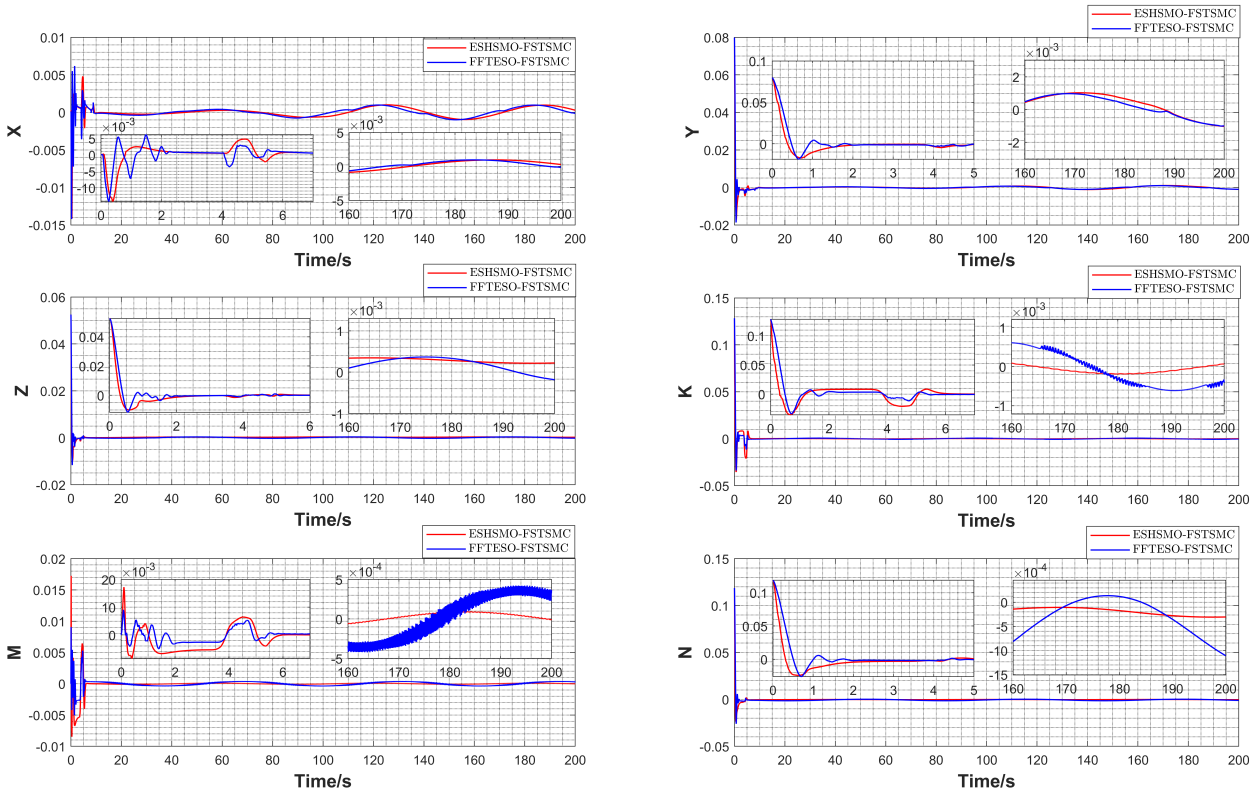


Figure 9. Observation error of lumped disturbance under ESHSMO-FSTSMC and FFTESO-FSTSMC. ESHSMO-FSTSMC observation error of lumped disturbance (red line) and FFTESO-FSTSMC observation error of lumped disturbance (blue line). Moreover, note that the six degrees of freedom for surge, sway, heave, roll, pitch, and yaw are represented by the letters X, Y, Z, K, M, and N, respectively.

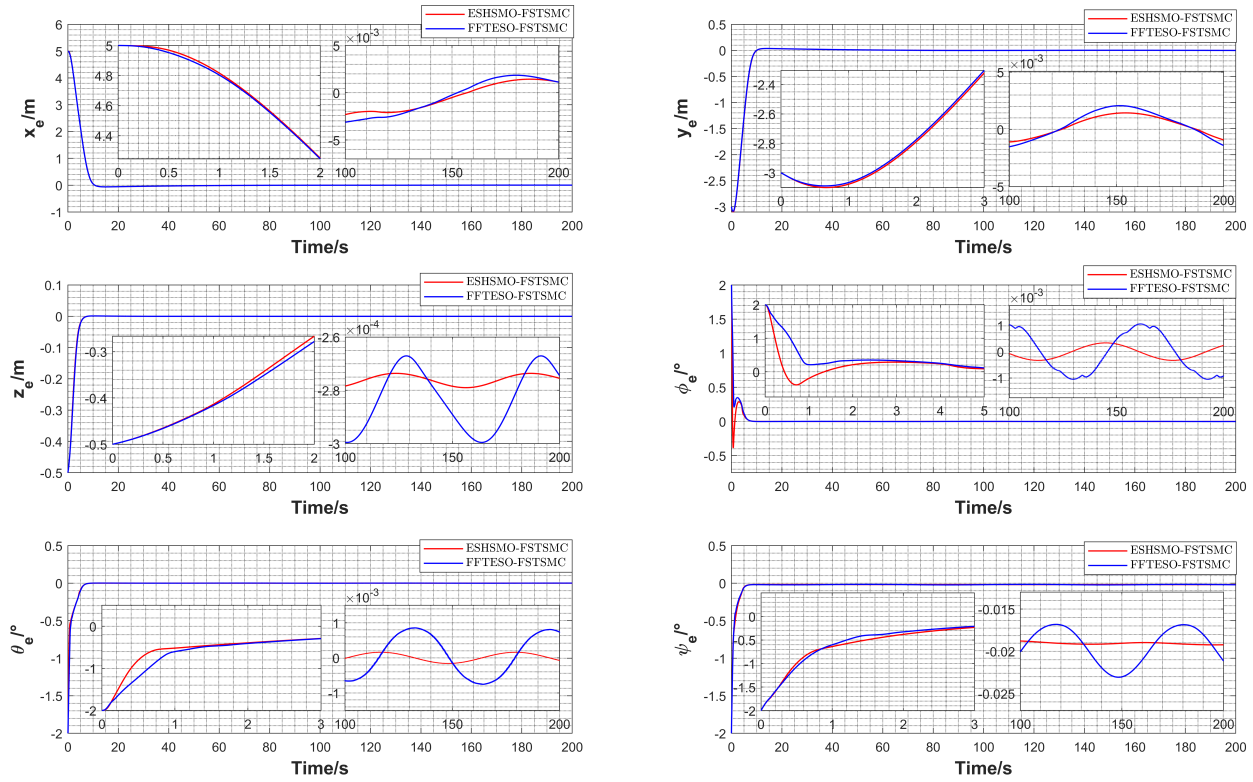


Figure 10. Trajectory tracking error under ESHSMO-FSTSMC and FFTESO-FSTSMC. ESHSMO-FSTSMC trajectory error (red line) and FTESO-FSTSMC trajectory error (blue line).

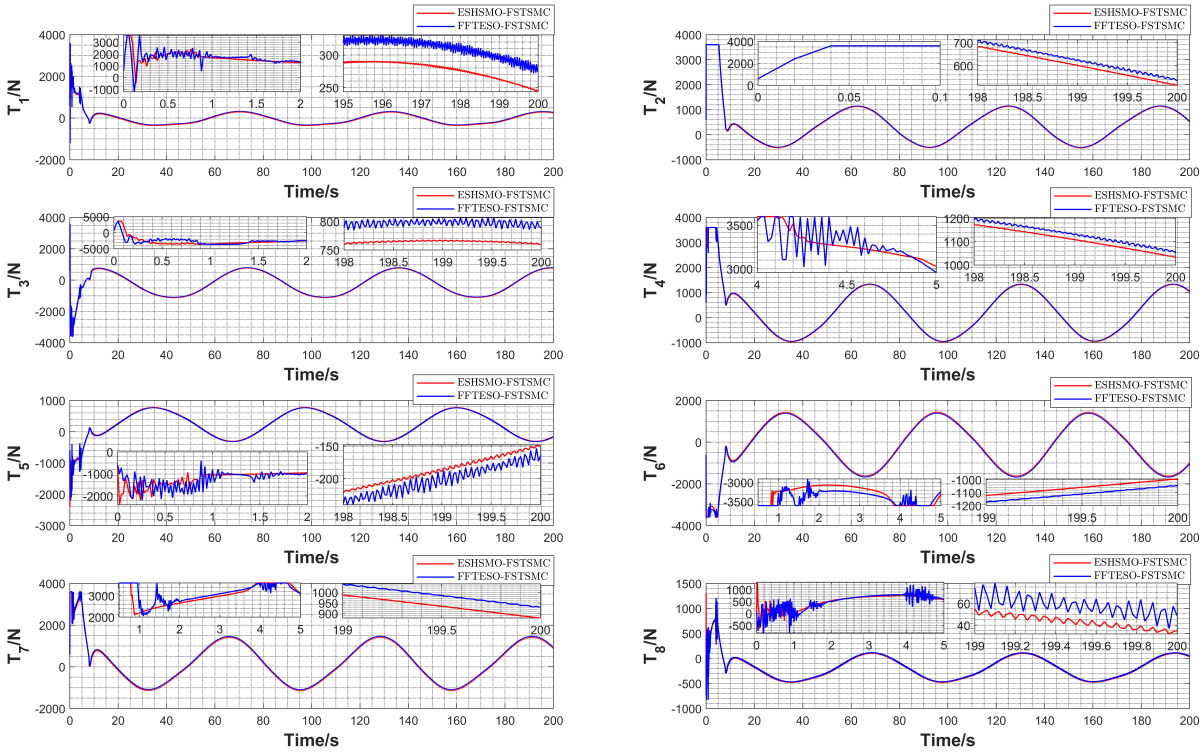


Figure 11. Thruster thrust under ESHSMO-FSTSMC and FFTESO-FSTSMC. ESHSMO-FSTSMC thruster (red line) and FTESO-FSTSMC thruster (blue line).

In Table 3, performance indicators including the root mean square error of lumped disturbance observation, root mean square error of ocean current velocity, root mean square error of trajectory tracking, observation convergence time and steady-state error are introduced to make a more detailed and accurate quantitative comparison between the ESHSMO-FSTSMC and FFTESO-FSTSMC.

Table 3. Quantitative comparison of ESHSMO-FSTSMC and FFTESO-FSTSMC trajectory tracking simulation results.

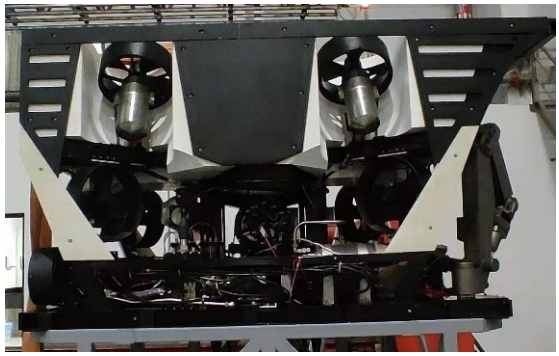
Performance Indicators	Control Scheme	x	y	z	ϕ	θ	ψ
Root mean square error of lumped disturbance observation	ESHSMO-FSTSMC	**0.0066**	**0.0066**	$\mathbf{4.6 \times 10^{-5}}$	$\mathbf{1.1 \times 10^{-4}}$	$\mathbf{2.3 \times 10^{-5}}$	$\mathbf{1.2 \times 10^{-4}}$
	FFTESO-FSTSMC	0.0094	0.0093	1.5×10^{-4}	6.0×10^{-4}	6.2×10^{-5}	5.3×10^{-4}
Root mean square error of ocean current velocity observation	ESHSMO-FSTSMC	7.9×10^{-4}	**0.0023**	**0.0014**	**0.0035**	8.9×10^{-4}	**0.0031**
	FFTESO-FSTSMC	$\mathbf{7.4 \times 10^{-4}}$	0.0026	0.0016	0.0042	$\mathbf{5.4 \times 10^{-4}}$	0.0039
Root mean square error of trajectory tracking	ESHSMO-FSTSMC	**0.6417**	**0.4050**	**0.0440**	**0.0686**	**0.0926**	0.0984
	FFTESO-FSTSMC	0.6427	0.4075	0.0447	0.0958	0.1047	**0.0975**
Convergence time	ESHSMO-FSTSMC	**8.76**	**8.22**	**5.34**	**4.78**	**4.82**	**4.32**
	FFTESO-FSTSMC	8.78	8.26	5.40	5.18	5.00	4.36
Steady-state error	ESHSMO-FSTSMC	0.00112	**−0.00091**	−0.00027	**0.00024**	$\mathbf{-7.2 \times 10^{-5}}$	**−0.019**
	FFTESO-FSTSMC	0.00112	−0.00141	−0.00027	−0.00092	0.00073	−0.021

The model mismatch caused by external disturbances and model uncertainties needs to increase the control gain to improve the robustness of the controller. This is usually detrimental to the overall control effect, such as causing excessive energy consumption, reducing stability margin, and even stimulating unmodeled characteristics. Therefore, the observer becomes an important part of the control scheme in the model mismatched system. From Figure 7, it is easy to know that both ESHSMO-FSTSMC and FFTESO-FSTSMC can successfully achieve 3D trajectory tracking with good robustness in the presence of current velocity disturbance and lumped disturbance. Figures 8 and 9 reflect that both ESHSMO and FFTESO can accurately approximate the disturbance with ESHSMO having a smoother observation effect and almost no chattering phenomenon due to the existence of higher-order sliding mode term Ξ. It can be found from Figure 10 that both ESHSMO-FSTSMC and FFTESO-FSTSMC have good trajectory tracking control performance, while a smaller oscillation amplitude can be obtained using ESHSMO-FSTSMC. In the case of the same control approach, this is because the observer has a more accurate and smooth observation curve. In Figure 11, it is easy to find that the thrust curve of ESHSMO-FSTSMC is smoother in the initial phase of trajectory tracking, while the chattering phenomenon is further suppressed in the stable stage of trajectory tracking. These phenomena indicate that the introduction of the sliding mode term can effectively enhance the robustness of the observer and suppress the high-frequency interference caused by high bandwidth. The above results show that ESHSMO-FSTSMC is more suitable with the output requirements of the thruster under the practical conditions. Table 3 compares quantitatively the control effects of ESHSMO-FSTSMC and FFTESO-FSTSMC, and ESHSMO-FSTSMC has a smaller root mean square error of lumped disturbance observation and ocean current velocity observation in the largest number of degrees of freedom. In general, ESHSMO-FSTSMC has a slight advantage in the root mean square error of trajectory tracking, convergence time and steady-state error. Based on the above simulation results, both ESHSMO-FSTSMC and FFTESO-FSTSMC achieve good trajectory tracking control performance under ocean velocity disturbance and lumped disturbance, and ESHSMO has achieved better results in chattering suppression, observation accuracy and convergence time. It is worth mentioning that ESHSMO-FSTSMC has a smoother thrust output, which is more suitable for the application requirements of UUV.

5.3. Experimental Verification

In order to further verify the feasibility of the trajectory tracking control scheme proposed in this paper, two sets of experiments have been conducted in a water pool: namely, the directional control and depth control experiment without external disturbances and the positioning control experiment with external disturbances. The UUV, the water pool and the control panel of the current generation system are shown in Figure 12.

In the directional control and depth control experiment, the initial heading is 316°, the target heading angle is set to 300°, the initial depth is 1.86 m, and the target depth is set to 2.86 m. The experiment results are shown in Figure 13. It can be seen that the steady-state error of directional control is less than 0.02°, and the steady-state error of depth control is less than 0.025 m, which indicates that the control scheme proposed in this paper can realize the high-precision control of UUV. In addition, the experiment verifies that the higher-order sliding mode technique in the control scheme can effectively weaken chattering and satisify the limitations of UUV thruster.



(**a**)



(**b**)

Figure 12. The UUV, the water pool and the control panel of the current generation system. (**a**) The UUV. (**b**) The water pool and the control panel of the current generation system.

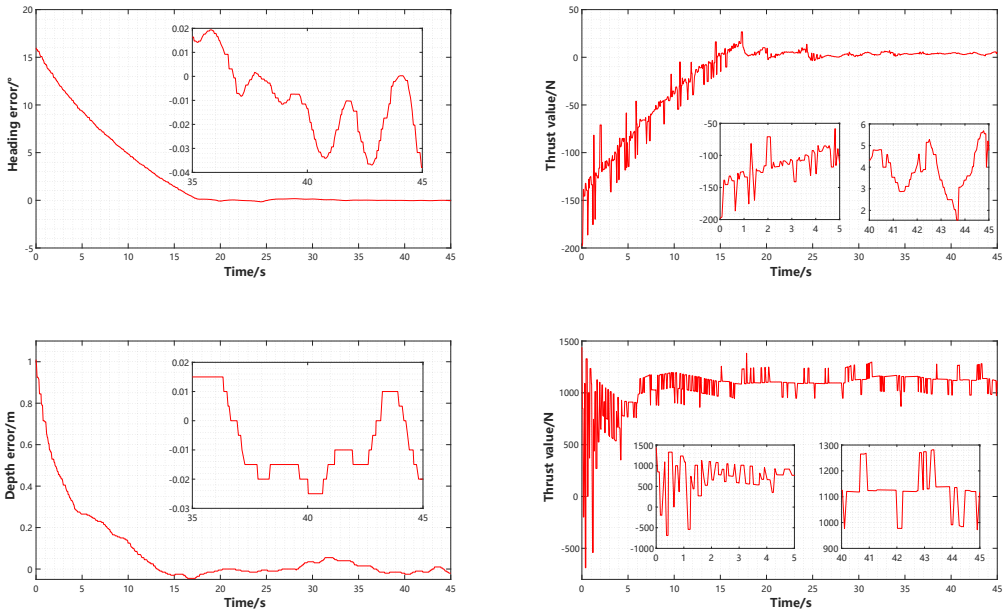


Figure 13. The directional control (upper) and depth control (bottom) experiment result.

In the positioning control experiment, the experiment pool is equipped with the current generation system, which can form a horizontal uniform current field, as shown in Figure 12. The current velocity can be adjusted by setting the system rotation frequency. During the experiment, the rotation frequency of the system is set to 30 Hz, generating a current of approximately 0.35 m/s. The detailed positioning experiment setup is shown in Figure 14. A fixed QR code with a side length of 15 cm is placed in the pool as a set point

for positioning control. At the same time, the inertial coordinate I is set at this point, where the x direction of the inertial coordinate system I is the same as the direction of the current. The UUV equipped with optical positioning equipment is set to move to the set point in the horizontal plane and remain in this position for a certain time. The positioning control results are shown in Figures 15 and 16. Due to the high-precision characteristics of the super-twisting sliding mode, the proposed control scheme has achieved good positioning performance with the steady-state error of the x direction and the steady-state error of the y direction as 0.05 m and 0.048 m, respectively. The observation steady-state errors of x, u, y and v in the system state vector $\boldsymbol{x}_1$ of Equation (11) can all converge accurately. According to the proof of Equation (26), it can be found that as long as the observer can achieve effective estimation of $\boldsymbol{x}_1$, it also can achieve effective estimation of current velocity and lumped disturbance. Among them, the current velocity observation $\hat{u}_f$ in the x direction basically fluctuates between 0.25 and 0.4 m/s, with a mean of 0.3133 m/s, and the mean of the lumped disturbance observation $\hat{\boldsymbol{\tau}}_D$ is 270.5 N. The mean of the current velocity disturbance $\hat{v}_f$ in the y direction is -0.1151 m/s, and the mean of the lumped disturbance observation $\hat{\boldsymbol{\tau}}_D$ is -12.38 N. The relative error between the current velocity observation $\hat{u}_f$ and the velocity of the generated current in the x direction is 10.49%. This indicates that ESHSMO has achieved good observation results in practical applications. In summary, the ESHSMO-FSTSMC control scheme proposed in this paper can effectively deal with external disturbances in the real scene, and it has good control performance and strong robustness.

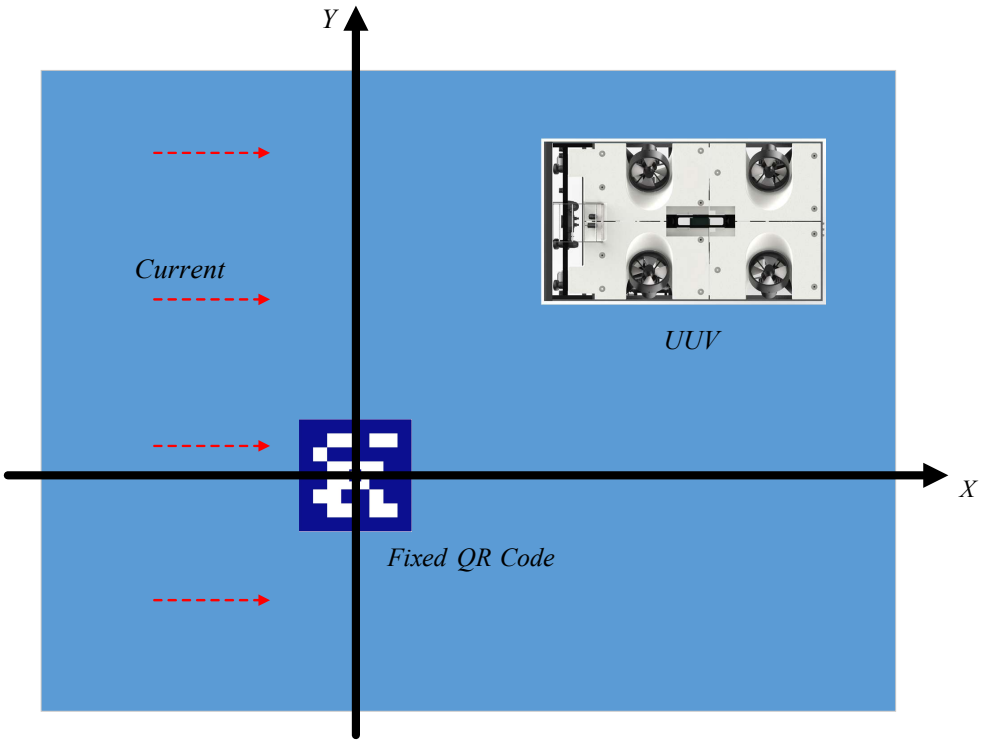


Figure 14. The positioning experiment setup.

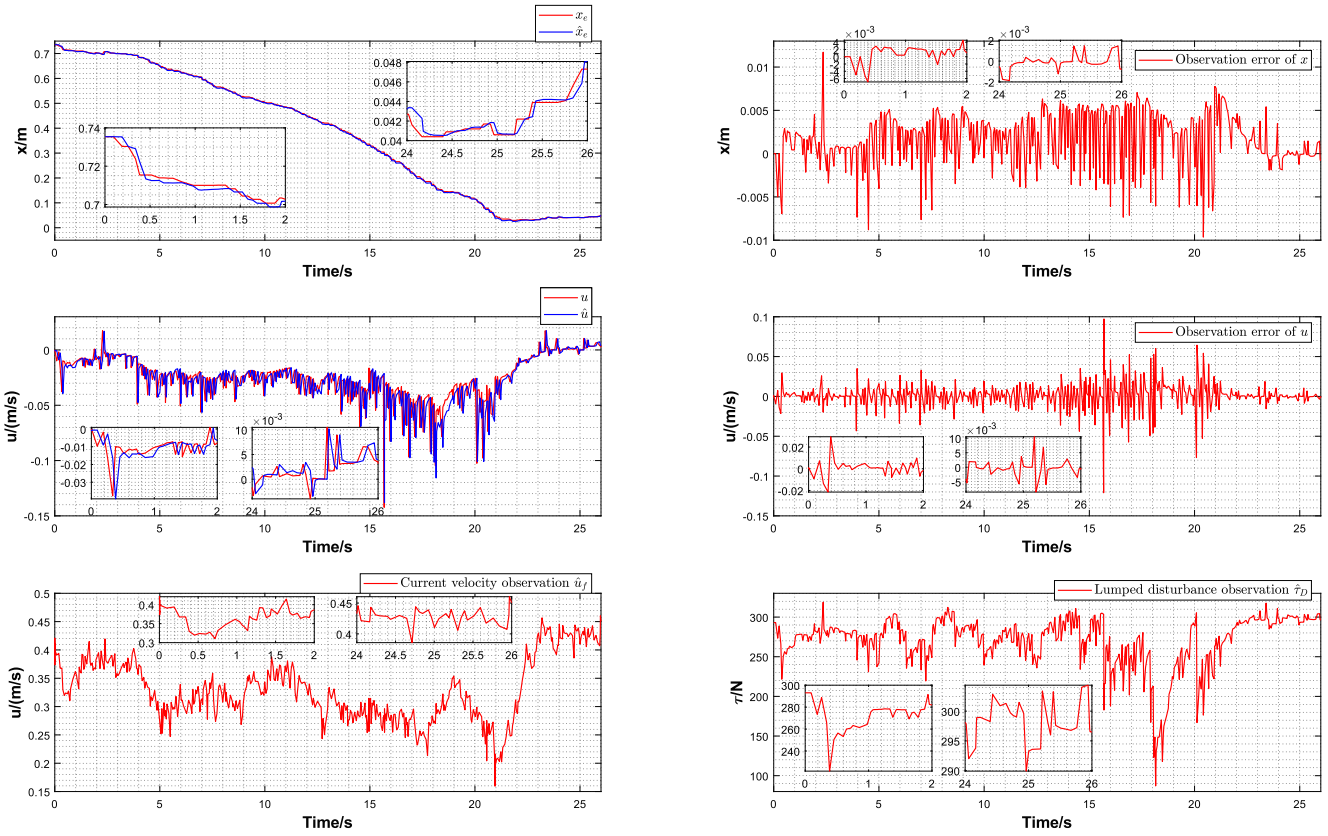


Figure 15. The x direction positioning control experiment result. Position, position observation and position observation error (upper), velocity, velocity observation and velocity observation error (middle), current velocity observation and lumped disturbance observation (bottom).

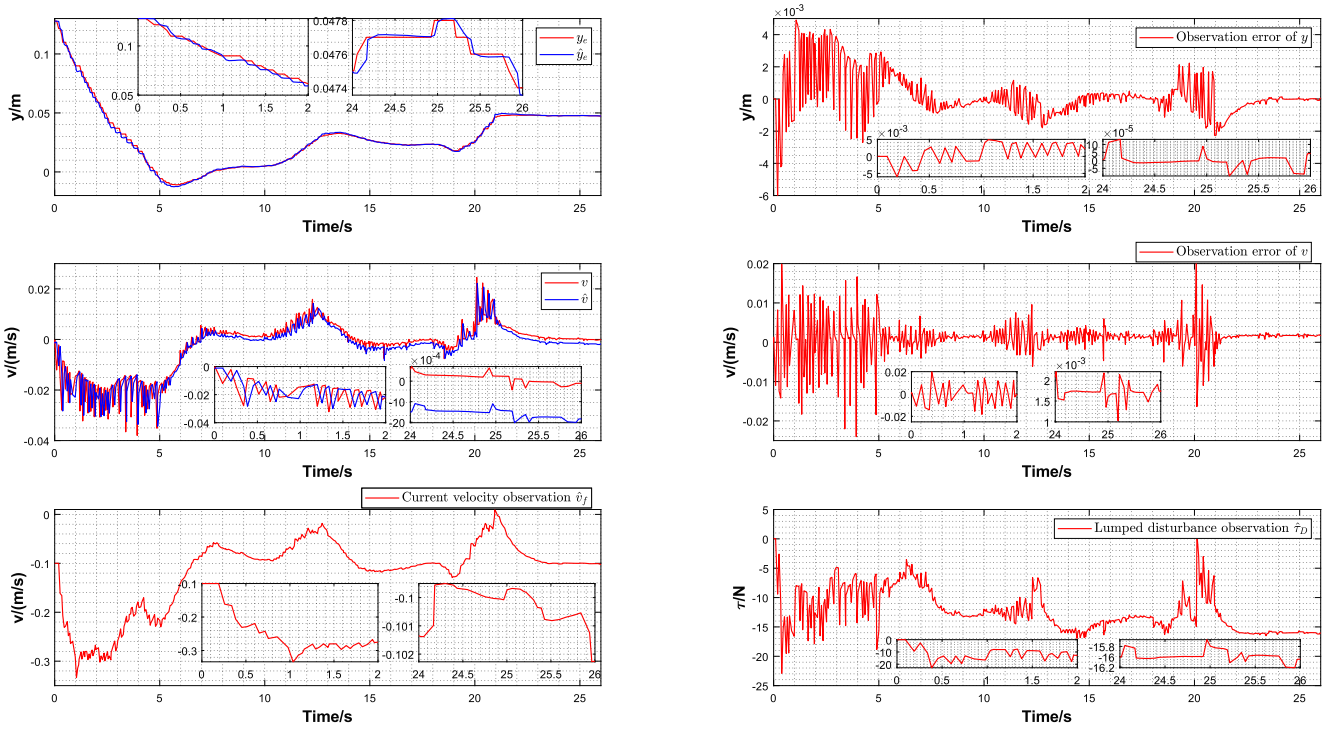


Figure 16. The y direction positioning control experiment result. Position, position observation and position observation error (upper), velocity, velocity observation and velocity observation error (middle), current velocity observation and lumped disturbance observation (bottom).

6. Conclusions

In this paper, a trajectory tracking control scheme including a fast finite-time super-twisting sliding mode control approach and an extended state higher-order sliding mode observer for UUVs is proposed and proven in detail. The numerical simulation and experiment verify that the proposed control scheme can effectively compensate the external disturbances and the model uncertainties, and it can attenuate the chattering of the control output and successfully control the UUV to perform the high-precision trajectory tracking task. Compared with STISMC, the addition of the fast term in FSTSMC provides advantages in tracking performance, chattering suppression and convergence speed. By using the higher-order sliding mode term, ESHSMO can further attenuate chattering compared with FFTESO, and more quickly and accurately estimate external disturbances and model uncertainties. In general, ESHSMO-FSTSMC successfully achieves the high control precision, the smaller chattering, the disturbance compensation and the fast finite-time convergence in UUV trajectory tracking. The future research and validation will focus on the adaptive tuning of control parameters and ocean experimental verification of the proposed control scheme.

Author Contributions: Conceptualization, L.G. and W.L.; methodology, L.G. and L.L.; software, L.G.; validation, L.G. and J.X.; funding acquisition, W.L.; resource, K.Z. and Y.Z.; writing—original draft preparation, L.G.; writing—review and editing, L.G., W.L. and L.L. All authors have read and agreed to the published version of the manuscript.

Funding: This research was funded in part by the National Science Foundation of China (project number 61903304), in part by the Fundamental Research Funds for the Central Universities (project number 3102020HHZY030010) and in part by the 111 Project under grant number B18041.

Institutional Review Board Statement: Not applicable.

Informed Consent Statement: Not applicable.

Data Availability Statement: The data presented in this study are available by sending a request to 2019100504@mail.nwpu.edu.cn.

Conflicts of Interest: The authors declare no conflicts of interest.

Abbreviations

The following abbreviations are used in this manuscript:

FSTSMC	Fast finite-time super-twisting sliding mode control
ESHSMO	Extended state higher-order sliding mode observer
UUV	Unmanned underwater vehicle
PID	Proportion integration differentiation
AUV	Autonomous underwater vehicle
ESO	Extended state observer
STISMC	Super-twisting integral sliding mode control
FFTESO	Fast finite-time extended state observer

References

1. Ali, N.; Tawiah, I.; Zhang, W. Finite-time extended state observer based nonsingular fast terminal sliding mode control of autonomous underwater vehicles. *Ocean Eng.* **2020**, *218*, 108179. [CrossRef]
2. Zhang, W.; Wu, W.; Li, Z.; Du, X.; Yan, Z. Three-Dimensional Trajectory Tracking of AUV Based on Nonsingular Terminal Sliding Mode and Active Disturbance Rejection Decoupling Control. *J. Mar. Sci. Eng.* **2023**, *11*, 959. [CrossRef]
3. Lv, T.; Zhou, J.; Wang, Y.; Gong, W.; Zhang, M. Sliding mode based fault tolerant control for autonomous underwater vehicle. *Ocean Eng.* **2020**, *216*, 107855. [CrossRef]
4. Mu, W.; Wang, Y.; Sun, H.; Liu, G. Double-Loop Sliding Mode Controller with An Ocean Current Observer for the Trajectory Tracking of ROV. *J. Mar. Sci. Eng.* **2021**, *9*, 1000. [CrossRef]
5. Elmokadem, T.; Zribi, M.; Youcef-Toumi, K. Terminal sliding mode control for the trajectory tracking of underactuated Autonomous Underwater Vehicles. *Ocean Eng.* **2017**, *129*, 613–625. [CrossRef]

6. Nguyen, X.; Mehdi, G.; Hong, S. Constrained Nonsingular Terminal Sliding Mode Attitude Control for Spacecraft: A Funnel Control Approach. *Mathematics* **2023**, *11*, 247.
7. Nguyen, X.; Mehdi, G. Smooth, Singularity-Free, Finite-Time Tracking Control for Euler–Lagrange Systems. *Mathematics* **2022**, *10*, 3850.
8. Xuan-Mung, N.; Nguyen, N.P.; Pham, D.B.; Dao, N.N.; Nguyen, H.T.; Ha Le Nhu Ngoc, T.; Vu, M.T.; Hong, S.K. Novel gain-tuning for sliding mode control of second-order mechanical systems: Theory and experiments. *Sci. Rep.* **2023**, *13*, 10541–10541. [CrossRef]
9. Wang, W.; Yan, J.; Wang, H.; Ge, H.; Zhu, Z.; Yang, G. Adaptive MPC trajectory tracking for AUV based on Laguerre function. *Ocean Eng.* **2022**, *261*, 111870. [CrossRef]
10. Li, J.; Xia, Y.; Xu, G.; He, Z.; Xu, K.; Xu, G. Three-Dimensional Prescribed Performance Tracking Control of UUV via PMPC and RBFNN-FTTSMC. *J. Mar. Sci. Eng.* **2023**, *11*, 1357. [CrossRef]
11. Li, S.; Xu, C.; Liu, J.; Han, B. Data-driven docking control of autonomous double-ended ferries based on iterative learning model predictive control. *Ocean Eng.* **2023**, *273*, 113994. [CrossRef]
12. Long, C.; Qin, X.; Bian, Y.; Hu, M. Trajectory tracking control of ROVs considering external disturbances and measurement noises using ESKF-based MPC. *Ocean Eng.* **2021**, *241*, 109991. [CrossRef]
13. Zhang, J.; Xiang, X.; Lapierre, L.; Zhang, Q.; Li, W. Approach-angle-based three-dimensional indirect adaptive fuzzy path following of under-actuated AUV with input saturation. *Appl. Ocean Res.* **2021**, *107*, 102486. [CrossRef]
14. Yu, C.; Xiang, X.; Wilson, P.A.; Zhang, Q. Guidance-error-based robust fuzzy adaptive control for bottom following of a flight-style AUV with saturated actuator dynamics. *IEEE Trans. Cybern.* **2020**, *50*, 1887–1899. [CrossRef] [PubMed]
15. Miao, J.; Sun, X.; Chen, Q.; Zhang, H.; Liu, W.; Wang, Y. Robust Path-Following Control for AUV under Multiple Uncertainties and Input Saturation. *Drones* **2023**, *7*, 665. [CrossRef]
16. Che, G. Single critic network based fault-tolerant tracking control for underactuated AUV with actuator fault. *Ocean Eng.* **2022**, *254*, 111380. [CrossRef]
17. Xuan-Mung, N.; Golestani, M.; Hong, S.-K. Tan-Type BLF-Based Attitude Tracking Control Design for Rigid Spacecraft with Arbitrary Disturbances. *Mathematics* **2022**, *10*, 4548. [CrossRef]
18. Wan, J.; Liu, H.; Yuan, J.; Shen, Y.; Zhang, H.; Wang, H.; Zheng, Y. Motion Control of Autonomous Underwater Vehicle Based on Fractional Calculus Active Disturbance Rejection. *J. Mar. Sci. Eng.* **2021**, *9*, 1306. [CrossRef]
19. Lamraoui, H.C.; Qidan, Z. Path following control of fully-actuated autonomous underwater vehicle in presence of fast-varying disturbances. *Appl. Ocean Res.* **2019**, *86*, 40–46. [CrossRef]
20. An, L.; Li, Y.; Cao, J.; Jiang, Y.; He, J.; Wu, H. Proximate time optimal for the heading control of underactuated autonomous underwater vehicle with input nonlinearities. *Appl. Ocean Res.* **2020**, *95*, 102002. [CrossRef]
21. Zhou, Y.; Sun, X.; Sang, H.; Yu, P. Robust dynamic heading tracking control for wave gliders. *Ocean Eng.* **2022**, *256*, 111510. [CrossRef]
22. Liu, J.; Zhao, M.; Qiao, L. Adaptive barrier Lyapunov function-based obstacle avoidance control for an autonomous underwater vehicle with multiple static and moving obstacles. *Ocean Eng.* **2022**, *243*, 110303. [CrossRef]
23. Guo, J.; Wang, J.; Bo, Y. An observer-based adaptive neural network finite-time tracking control for autonomous underwater vehicles via command filters. *Drones* **2023**, *7*, 604. [CrossRef]
24. Zhao, J.; Qin, Y.; Hu, C.; Xu, G.; Xu, K.; Xia, Y. Robust Adaptive Backstepping Motion Control of Underwater Cable-Driven Parallel Mechanism Using Improved Linear Model Predictive Control. *J. Mar. Sci. Eng.* **2023**, *11*, 1173. [CrossRef]
25. Makavita, C.D.; Jayasinghe, S.G.; Nguyen, H.D.; Ranmuthugala, D. Experimental comparison of two composite MRAC methods for UUV operations with low adaptation gains. *IEEE J. Ocean. Eng.* **2020**, *45*, 227–246. [CrossRef]
26. Nguyen, X.; Mehdi, G. Energy-Efficient Disturbance Observer-Based Attitude Tracking Control With Fixed-Time Convergence for Spacecraft. *IEEE Trans. Aerosp. Electron. Syst.* **2023**, *59*, 3659–3668.
27. Golestani, M.; Zhang, W.; Yang, Y.; Xuan-Mung, N. Disturbance observer-based constrained attitude control for flexible spacecraft. *IEEE Trans. Aerosp. Electron. Syst.* **2022**, *59*, 963–972. [CrossRef]
28. Mehdi, G.; Seyed, M.; Saleh, M. Fixed-time control for high-precision attitude stabilization of flexible spacecraft. *Eur. J. Control* **2021**, *57*, 222–231.
29. Huang, B.; Yang, Q. Double-loop sliding mode controller with a novel switching term for the trajectory tracking of work-class ROVs. *Ocean Eng.* **2019**, *178*, 80–94. [CrossRef]
30. Labbadi, M.; Cherkaoui, M. Robust adaptive backstepping fast terminal sliding mode controller for uncertain quadrotor UAV. *Aerosp. Sci. Technol.* **2019**, *93*, 105306. [CrossRef]
31. Elmokadem, T.; Zribi, M.; Youcef-Toumi, K. Trajectory tracking sliding mode control of underactuated AUVs. *Nonlinear Dyn.* **2016**, *84*, 1079–1091. [CrossRef]
32. Levant, A. Higher Order Sliding Modes and Their Application for Controlling Uncertain Processes. Ph.D. Dissertation, Institute for System Studies of the USSR Academy of Science, Moscow, Russia, 1987.
33. Borlaug, I.G.; Pettersen, K.Y.; Gravdahl, J.T. Comparison of two second-order sliding mode control algorithms for an articulated intervention AUV: Theory and experimental results. *Ocean Eng.* **2021**, *222*, 108480. [CrossRef]
34. Manzanilla, A.; Ibarra, E.; Salazar, S. Super-twisting integral sliding mode control for trajectory tracking of an Unmanned Underwater Vehicle. *Ocean Eng.* **2021**, *234*, 109164. [CrossRef]

35. González-García, J.; Gómez-Espinosa, A.; García-Valdovinos, L.G.; Salgado-Jiménez, T.; Cuan-Urquizo, E.; Escobedo Cabello, J.A. Experimental Validation of a Model-Free High-Order Sliding Mode Controller with Finite-Time Convergence for Trajectory Tracking of Autonomous Underwater Vehicles. *Sensors* **2022**, *22*, 488. [CrossRef] [PubMed]
36. Li, X.; Ren, C.; Ma, S.; Zhu, X. Compensated model-free adaptive tracking control scheme for autonomous underwater vehicles via extended state observer. *Ocean Eng.* **2020**, *217*, 107976. [CrossRef]
37. Wu, C.; Dai, Y.; Shan, L.; Zhu, Z.; Wu, Z. Data-driven trajectory tracking control for autonomous underwater vehicle based on iterative extended state observer. *Math. Biosci. Eng. MBE* **2022**, *19*, 3036–3055. [CrossRef] [PubMed]
38. Kim, H.-H.; Lee, M.C.; Cho, H.-J.; Hwang, J.-H.; Won, J.-S. SMCSPO-Based Robust Control of AUV in Underwater Environments including Disturbances. *Appl. Sci.* **2021**, *11*, 10978. [CrossRef]
39. Hu, Q.; Jiang, B. Continuous Finite-Time Attitude Control for Rigid Spacecraft Based on Angular Velocity Observer. *IEEE Trans. Aerosp. Electron. Syst.* **2018**, *54*, 1082–1092. [CrossRef]
40. Li, S.; Du, H.; Lin, X. Finite-time consensus algorithm for multi-agent systems with double-integrator dynamics. *Automatica* **2011**, *47*, 1706–1712. [CrossRef]
41. Fossen, T.I. Marine Control Systems. Marine Cybernetics. 2002. Available online: http://kashti.ir/files/ENBOOKS/Marine%20control%20systems.pdf (accessed on 23 January 2024).
42. Abdurahman, B.; Savvaris, A.; Tsourdos, A. Switching LOS guidance with speed allocation and vertical course control for path-following of unmanned underwater vehicles under ocean current disturbances. *Ocean Eng.* **2019**, *182*, 412–426. [CrossRef]

Disclaimer/Publisher's Note: The statements, opinions and data contained in all publications are solely those of the individual author(s) and contributor(s) and not of MDPI and/or the editor(s). MDPI and/or the editor(s) disclaim responsibility for any injury to people or property resulting from any ideas, methods, instructions or products referred to in the content.